New Journal of Physics
The open-access journal for physics

Ultrafast optical excitations of metallic nanostructures: from light confinement to a novel electron source

Claus Ropers[1], Thomas Elsaesser[1], Giulio Cerullo[2], Margherita Zavelani-Rossi[2] and Christoph Lienau[3,4]

[1] Max-Born-Institut für Nichtlineare Optik und Kurzzeitspektroskopie, Max-Born-Street 2A, 12489 Berlin, Germany
[2] Dipartimento di Fisica, Politecnico di Milano, Piazza L da Vinci 32, 20133 Milano, Italy
[3] Carl von Ossietzky Universität, Institut für Physik, 26111 Oldenburg, Germany
E-mail: christoph.lienau@uni-oldenburg.de

New Journal of Physics **9** (2007) 397
Received 4 June 2007
Published 31 October 2007
Online at http://www.njp.org/
doi:10.1088/1367-2630/9/10/397

Abstract. Combining ultrafast coherent spectroscopy with nano-optical microscopy techniques offers a wealth of new possibilities for exploring the structure and function of nanostructures. In this paper, we describe newly developed nano-optical methods based on short-pulse laser sources with durations in the 10 fs regime. These techniques are used to unravel some of the intricate dynamics of elementary excitations in metallic nanostructures. Specifically, we explore light localization and storage in plasmonic crystals, demonstrate field enhancement and second harmonic generation from metallic nanotips and describe a novel nanometre-sized source of electron pulses. The rapid progress in this area offers exciting new prospects for probing and controlling electron dynamics in metallic nanostructures with femtosecond temporal and nanometre spatial resolution.

[4] Author to whom any correspondence should be addressed.

PII: S1367-2630(07)51915-4

Contents

1. Introduction

The optical properties of metals are extraordinary in many respects. The most apparent feature is certainly their high reflectivity, which, for some metals, spans from the far infrared to the ultraviolet spectral ranges. This reflectivity can be traced back to the large density of mobile conduction electrons that react to incoming light fields and prevent them from penetrating the metal. Such exclusion effects take place very close to the surface, in a narrow region known as the 'skin depth', a thin layer of approximately 10 nm in thickness.

Light impinging on a metal surface induces charge and current oscillations within the skin depth, which in-turn create optical fields near the surface that act back on the charges. This can result in combined resonant modes of the electron motion with a surface-bound electromagnetic field. The relevant timescales of such resonances are usually exceedingly short, typically in the range of femtoseconds.

Depending on the particular geometry, these excitations may have markedly different characteristics. For example, surface plasmon polaritons (SPPs) [1] are delocalized waves traveling along a metal surface and can possess spatial coherence lengths up to several millimetres for near-infrared light and metals like gold or silver [2, 3]. On the other hand, sharp edges or other highly curved geometries, e.g. nanometre scale metal clusters, lead to localized surface plasmons, highly spatially concentrated resonances in which the electromagnetic fields may far exceed those illuminating the structure.

Due to this wide range of properties from field localization to mesoscopic surface-bound optical transport, the study of surface plasmons has developed from a topic of fundamental research to a focus of various novel technological applications in opto-electronics, biology and medicine. Surface plasmons are used, for example, to enhance Raman scattering [4], molecular fluorescence [5] and the output efficiency of solid state light emitters [6] and Terahertz lasers [7]. Commercial surface plasmon resonance ellipsometers [8] are capable of tracing minute amounts of a substance, e.g. in the detection of protein monolayers [9] or to monitor antibody reactions.

An exciting theme in 'plasmonics' that is expected to make the leap to technological relevance in the near future is the control of light propagation and localization on the

nanoscale [10]–[13]. A prominent early example was the achievement of very high optical transmissivity through periodic arrays of very small subwavelength apertures in thin metal sheets [14]. These periodically-patterned film structures are ideal model systems that merge the concepts known from photonic crystals [15] with the exceptional material properties of metals to form 'plasmonic crystals'.

The SPPs excited in these structures are strongly coupled to the optical far-field, which limits their lifetime to few tens of femtoseconds [16]–[18]. This will restrict their use in certain optical elements and calls for a better understanding of ways to control these lifetimes. Equally important are new experimental tools for probing and manipulating the elementary excitations of metallic nanostructures. Due to these short lifetimes, time-resolved studies are challenging and require extremely short laser pulses [19]. In addition, unavoidable size fluctuations in nanostructure ensembles make studies of individual nanostructures highly desirable, often requiring imaging and spectroscopy techniques with ultrahigh spatial resolution [19]–[21].

It is the aim of this paper to describe recent experimental progress in combining ultrafast coherent laser spectroscopy and nano-optical imaging techniques for probing the elementary excitations of metallic nanostructures. Three specific examples are discussed. First, it is shown how the interplay between light localization and SPP propagation gives rise to the resonant light transmission through metallic nanoarrays. Then, the spatial localization of ultrashort light pulses is used to enhance second harmonic generation (SHG) from metallic nanotips and produce an isolated light nanosource that can be employed in background-free sub-wavelength imaging. Finally, we demonstrate a nanometre-sized electron source based on the field enhancement of sub-10 fs pulses at the very end of a metal nanotip. The physics underlying the electron generation is elucidated, and perspectives for novel applications are discussed.

2. Experimental

2.1. Laser sources

For the experimental studies on enhanced transmission through metallic nanostructures and for localized electron generation, we used two commercial 80 MHz repetition rate broadband Ti : sapphire oscillators (Femtolasers), delivering optical pulses at a center wavelength of 800 nm with pulse durations of 11 and 7 fs, respectively. Typical spectra of the two lasers are shown in figures 1(a) and (c). The large spectral width of these lasers, in combination with their high brightness, makes them exceptionally useful for the spectroscopic experiments with high angular resolution described in section 3.1. The time-dependent electric field $E(t)$ of the generated light pulses has been characterized in interferometric autocorrelation (IAC) measurements [22]. IAC traces are shown in figures 1(b) and (d), respectively. The full-width-at-half-maximum (FWHM) of the IAC shown in figure 1(d) amounts to 10.0 fs, which corresponds to a pulse duration of 6.5 fs assuming a hyperbolic secant pulse shape [23]. The data in figure 1(b) yield a longer pulse duration of approximately 11 fs.

As a unique electric field reconstruction from IAC traces is not possible, we have characterized the laser pulses [23] by both SPIDER ('spectral phase interferometry for direct electric-field reconstruction') [24] and FROG ('frequency-resolved optical gating') [25]. Both methods allow for a reconstruction of the (relative) spectral phase $\phi(\omega) = \arg(\tilde{E}(\omega))$ of a light pulse, where $\tilde{E}(\omega)$ is the Fourier transform (frequency representation) of $E(t)$. The phase curves are plotted in figures 1(a) and (c) as gray lines. From these measurements, the full

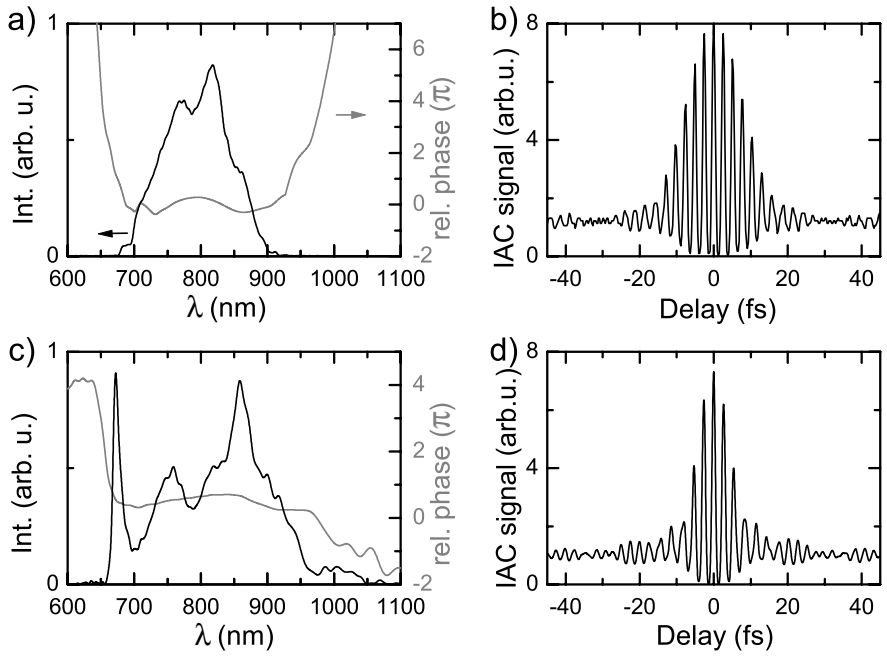

Figure 1. (a) Optical spectrum (black) and relative spectral phase (gray) of the 10 fs Ti : sapphire laser oscillator used for the experiments with metal nanogratings. (b) IAC measured for this laser. (c)–(d) Corresponding data for the 7 fs laser oscillator (Femtolasers Rainbow) used for the electron generation experiments.

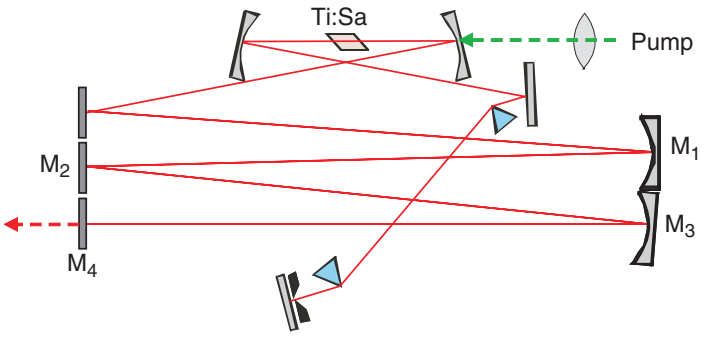

Figure 2. Scheme of the stretched-cavity mode-locked Ti : sapphire oscillator used for the experiments.

time dependent electric field of a laser is obtained by inverse Fourier transformation. The only information not delivered by these characterizations is the absolute phase of the electric field [26, 27], which is not directly relevant for the experiments discussed here.

For the second-harmonic (SH) experiments, we have used a home-made stretched-cavity Kerr-lens mode-locked Ti : sapphire oscillator. The laser setup is shown in figure 2; the cavity length of a 'standard' oscillator with a 5 mm Ti : sapphire rod is extended by introducing in one arm a 1 : 1 folded intracavity telescope, consisting of two −2000 mm radius concave mirrors

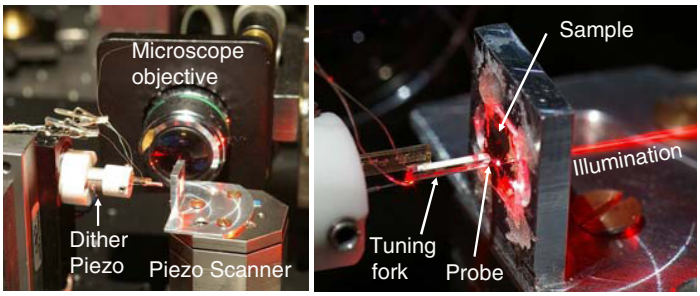

Figure 3. Photographs of the central part of the near-field microscope. The microscope is based on a hardware-linearized scanner with a scan range of $5 \times 5 \times 5\,\mu\text{m}^3$ and employs a horizontal tip orientation.

(mirrors M1 and M3) [28, 29]. The telescope has a unity *ABCD* matrix so as to keep the optical stability limits of the cavity unchanged. The laser generates 25 fs pulses at 800 nm with 26 MHz repetition rate and a maximum output power of 500 mW, corresponding to a pulse energy of 20 nJ. This source results, for a given average laser power, in a fourfold increase in pulse energy with respect to a standard 100 MHz oscillator, significantly boosting the SHG for a safe power level incident on the metal tip. Although even longer resonators with a repetition rate down to 5 MHz have been reported in the literature [30], our system represents an excellent compromise in terms of stability and reliability.

2.2. Near-field microscopes

The linear optical properties of metallic nanoarrays are studied by both conventional far-field white-light spectroscopy and near-field scanning optical microscopy (NSOM). These NSOM experiments are performed at room temperature with a home-built microscope (figure 3), based on a hardware-linearized piezo scanner ('Picocube', Physik Instrumente) with a three-dimensional scan range of $5 \times 5 \times 5\,\mu\text{m}^3$ and a capacitive position detection with a precision of better than 0.5 nm.

The distance between the tip and the sample is regulated by a shear-force feedback system [31] employing a tuning fork sensor [32, 33]. The tips are glued on one tine of a quartz tuning fork, extending past the end of the fork by roughly 100 μm. The tuning fork is mechanically excited at its resonant frequency ($\sim$32.8 kHz) by applying a small ac voltage to a tube piezo, on which it is mounted (denoted as 'dither-piezo'). The current induced between the two electrical tuning fork contacts by the mechanical oscillation is picked up, amplified by a transimpedance amplifier (gain up to $1\,\text{GV}\,\text{A}^{-1}$) and detected with a lock-in-amplifier. The experiments are performed with oscillation amplitudes of about 1 nm to achieve high spatial resolution in the image while maintaining an amplitude detection noise ratio of less than 5×10^{-3}. In order to avoid mechanical vibrations from the set-up, the microscope was placed on a passive vibration insulation table inside a sound insulation housing.

For the electron experiments described in section 3.3, this microscope is installed inside a high vacuum chamber operating at a base pressure of about 10^{-7} mbar. The chamber is evacuated using a magnetic bearing turbomolecular pump (BOC Edwards), which is kept operating during the course of the experiments.

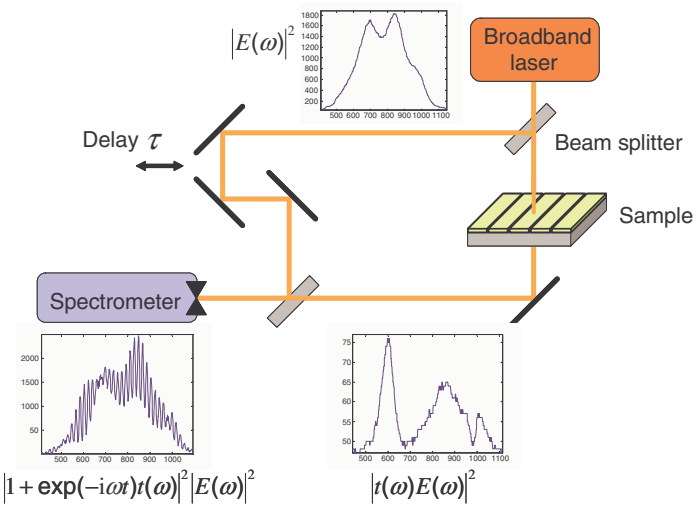

Figure 4. Spectral interferometry. The broadband laser pulses are split and sent through the two arms of a Mach–Zehnder interferometer. The spectral interferogram (bottom left) between the reference pulse (top) and the pulse transmitted through the investigated sample (bottom right) shows oscillations which can be adjusted by a temporal delay τ.

For the SH imaging experiments described in section 3.2, we used a home-built scattering NSOM (s-NSOM) consisting of a modified atomic force microscope (AFM) operated in the intermittent contact mode (or 'tapping mode') [34]. We employ commercial metal-coated cantilevered silicon tips (model ContPt from Nanosensors) which are glued on a quartz tuning fork that becomes the force sensor instead of the cantilever itself. The tuning fork is glued on to a dither piezo operating at amplitudes ranging from 3 to 30 nm peak-to-peak. The tuning fork signal is fed to an amplitude demodulator (Nanosurf, Model EasyPLL). For the feedback loop, we use a standard analog controller which drives the z-axis of an x–y–z-piezo-scanner stage (Physik Instrumente, Germany).

2.3. Spectral interferometry (SI)

In the far-field optical studies of metallic nanoarrays, we use the technique of SI [35] to fully characterize the angle-dependent linear transmissivity $t(\omega)$ of these samples. This complex function connects the incident and transmitted laser fields via

$$E_{\text{out}}(\omega) = t(\omega)E_{\text{in}}(\omega), \tag{1}$$

and its magnitude squared gives the usual transmission spectrum $T(\omega) = |t(\omega)|^2$.

In SI [35], a broadband optical pulse is sent through two arms of a dispersion-balanced Mach–Zehnder interferometer (see figure 4). The light transmitted through the investigated medium is brought to interference with an undisturbed reference field from the same source. The superposition of both fields is spectrally resolved, and the intensity of this spectral interferogram is given as

$$S(\omega) = |\exp(-i\omega\tau) + t(\omega)|^2|E_{\text{in}}(\omega)|^2. \tag{2}$$

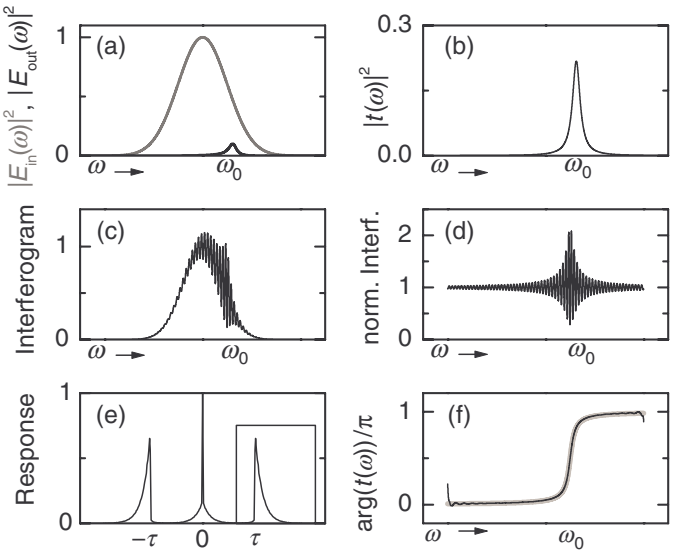

Figure 5. Intermediate steps in the phase retrieval algorithm. As an example, a Lorentzian transmission resonance at a frequency ω_0 is shown. (a) Spectrum of the incoming and the transmitted fields. (b) Normalized transmission spectrum. (c) Spectral interferogram. (d) Normalized spectral interferogram. (e) Magnitude of the Fourier transform of the normalized spectral interferogram. (f) Retrieved (black) and exact (gray) spectral phase of the Lorentzian resonance.

The rapid interference oscillations in the interferogram are due to the first term of this product, and the fringe spacing can be adjusted by the choice of the delay τ in the reference arm. A phase reconstruction for $t(\omega)$, illustrated by some intermediate steps shown in figure 5, proceeds as follows: (i) the interferogram (c) is divided by the incoming spectrum $|E_{\mathrm{in}}(\omega)|^2$ (gray curve in (a)), leaving a term that, after expansion, reads (see (d))

$$\frac{S(\omega)}{|E_{\mathrm{in}}(\omega)|^2} = 1 + |t(\omega)|^2 + 2\mathrm{Re}(t(\omega)\exp(-\mathrm{i}\omega\tau)). \tag{3}$$

(ii) A Fourier transform of this expression results in a component centered around zero, and two components that are shifted in the time domain by a positive and a negative value of the delay τ. The magnitude of its Fourier transform is shown in figure 5(e). (iii) Selecting only the positive time component with a time-window filter [35] and back-transforming it into the frequency domain yields the complex $t(\omega)\exp(-\mathrm{i}\omega\tau)$. Of this expression, the argument can be immediately evaluated numerically, compensating for the linearly increasing phase contribution $\omega\tau$ (figure 5(f, black line)). For comparison, the well-known π-phase change of a Lorentzian resonance is plotted as the thick gray line. Small deviations of the retrieved phase information from the ideal phase curve are only visible at the edges of the frequency domain, resulting from a bandwidth restriction in the numerical calculations.

A major prerequisite for SI is a good visibility of the fringes in the interferogram. Mechanical fluctuations often degrade the fringe visibility. One solution to this problem is an active stabilization of the interferometer with a frequency-stable cw-laser reference, e.g. a He-Ne-laser. In our case, we have largely reduced the effects of mechanical fluctuations by using a fast line-scan charge-coupled-device (CCD) camera after the monochromator. This camera is

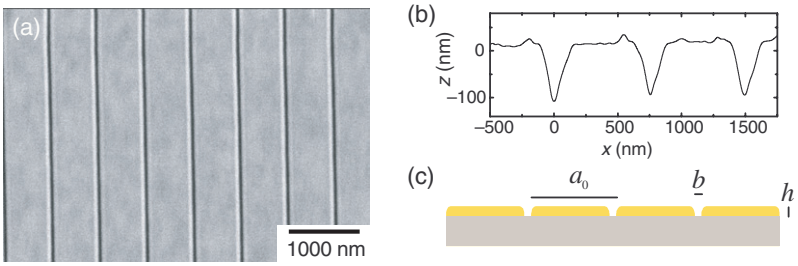

Figure 6. The investigated periodically patterned thin-film gratings. (a) Scanning electron micrograph of a one-dimensional slit array in a gold film. (b) Cross-section as measured with the shear-force topography detection. (c) Definitions of the structural parameters lattice period a_0, slit width b and film thickness h.

capable of integration times on the order of 1 ms, so that mechanical vibrations up to 1 kHz have little influence on the fringe visibility.

3. Results and discussion

3.1. Light localization and SPP excitations in metallic nanoarrays

Ever since the first experiments reported by Ebbesen *et al* [14], the surprising 'extraordinary' enhancement of the optical transmission through periodic arrays of nanometric holes or slits in metal films has been one of the most heavily debated topics in optics. The discussion of the underlying physical mechanisms has been highly controversial [36]–[40] and continues to attract broad interest [41].

It is the aim of this section to demonstrate that the combination of coherent optical techniques and spatially resolved near-field spectroscopic techniques yields a quite clear picture of the microscopic physical phenomena governing the linear optical properties of these arrays. In addition, new and interesting phenomena such as the sub-radiant suppression of SPP damping in nanoslit arrays are found [42].

As a model system, we investigate 150 nm thick gold films perforated by linear arrays of 50 nm wide nanoslits with a periods of $a_0 = 650$ and 750 nm (figure 6). The samples are fabricated by dry etching after e-beam patterning of a gold film grown on a flat sapphire substrate [16, 43].

Conventional angle-resolved linear transmission spectra of such an array (figure 7) show a pronounced enhancement of the transmission at certain resonance wavelengths. The corresponding optical frequencies are close to those expected for grating-coupling of monochromatic light at frequency ω_L, to SPP excitations at either the air–metal (AM) or sapphire/metal (SM) interface of a thin metal grating [1, 44]. The light is incident at an angle θ and with in-plane wavevector $k_{\|} = (\omega/c)\sin(\theta)$. These resonance frequencies can be estimated from the SPP dispersion relation on a planar metal–dielectric interface $\omega(\mathbf{k}_{SP}) = c|\mathbf{k}_{SP}|(\frac{\epsilon_m+\epsilon_d}{\epsilon_m\epsilon_d})^{1/2}$, energy conservation $\omega_L = \omega(\mathbf{k}_{SP})$ and momentum conservation. Here, ϵ_m and ϵ_d are the dielectric constants of the metal and dielectric, respectively. For slits, the in-plane SPP wavevector $\mathbf{k}_{SP}$ is oriented perpendicular to the slit axis and $k_{SP} = k_{\|} + p \cdot 2\pi/a_0$, where the integer p denotes the diffraction order. Consequently, the different transmission resonances are labeled as AM[p] and SM[p] for excitation of SPP modes at the air and sapphire side of the metallic film, respectively.

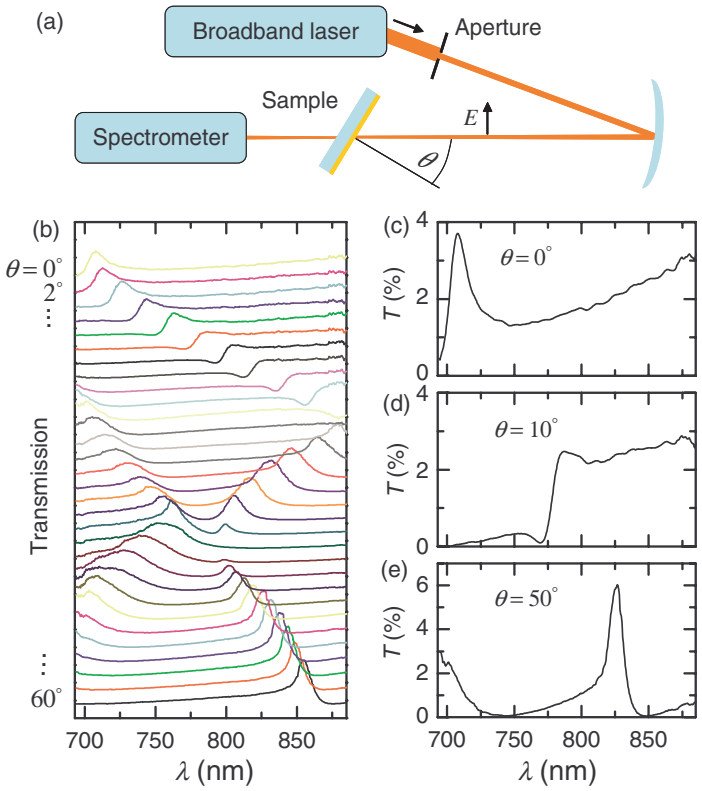

Figure 7. Angle-dependent transmission spectra of a gold nanoslit grating with $a_0 = 650\,\text{nm}$, $d = 150\,\text{nm}$ and $b = 50\,\text{nm}$ on a sapphire substrate. (a) Experimental set-up. The incident p-polarized laser light is narrowed down with an aperture and weakly focused on to the sample with a spherical mirror ($f = 30\,\text{cm}$). (b) Transmission spectra in steps of $\theta = 2^\circ$. (c)–(e) Three examples of transmission spectra for the indicated angles.

Based on such angle-resolved transmission spectra [14, 44], the energy dispersion of these resonances, their peculiar, asymmetric line shape [45, 46] and the nature of the elementary excitations underlying these resonances have been debated. Here, coherent optical experiments can give important additional information that may help in elucidating some of these issues. In our work, SI [35] is used to measure both amplitude and phase of the angle-dependent linear transmissivity $t(\omega)$, relating the electric field amplitudes of the incident $E_{\text{in}}(\omega)$ and transmitted pulses $E_{\text{out}}(\omega)$.

Experimental results at different angles of incidence are shown in figures 8(b)–(d), where the time structure of the transmitted pulses $E_{\text{out}}(t)$ is shown in the left panel. The normalized transmission $T(\omega) = |t(\omega)|^2$ and phase $\varphi = \arg(t(\omega))$ of the transmitted pulses is shown in the right panel. By continuously varying the angle of incidence one thus obtains full information on the band structure of these plasmonic crystals [42, 47, 48].

More detailed insight into the physical origin of these complex spectral variations can be obtained from a different representation of the results, shown in figure 9. Here, we plot in figures 9(a) and (b) the spectral intensity $|E(f)|^2 = |E(\omega/(2\pi))|^2$ and the time structure, respectively, of the field $E(t)$ of the pulse transmitted at an angle of 8° through the 650 nm

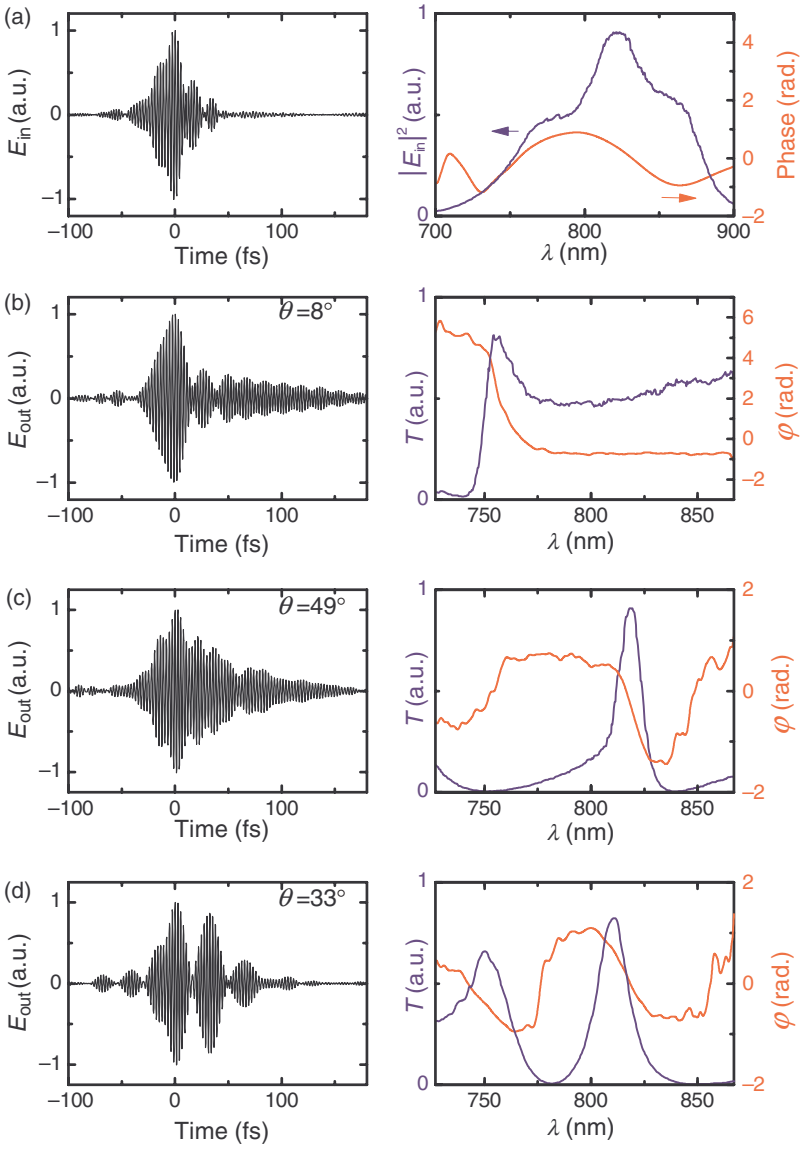

Figure 8. Incident and transmitted pulses through a 650 nm slit array. (a) Electric field transient (left graph), spectral intensity (blue) and spectral phase (red) of the incident pulses. (b)–(d) Transmitted pulse structures (left column), normalized transmission T (blue) and spectral phase φ (red) of the transmissivity for angles of incidence $\theta = 8^\circ$(b) (AM resonance), 49°(c) and 33°(d) (SM resonances).

slit array. Figure 9(c) shows the short-time Fourier transform function $W(f,t) = |\int \mathrm{d}t' g(t'-t)\, E(t') \exp(\mathrm{i}ft')|^2$, calculated with a Gaussian time window function $g(t) = \exp(-\frac{t^2}{2D^2})$ of width $D = 20$ fs.

This image shows quite clearly that the light spectrum transmitted through the nanoslit array undergoes a pronounced temporal evolution. Initially, it consists of an ultrafast burst covering essentially the entire spectrum of the incident laser. At later times, one finds exclusively the rather long-lived emission from resonant SPP excitations—in this example from the AM[−1] SPP excitation at around 390 THz (770 nm). In general, the time structure of the

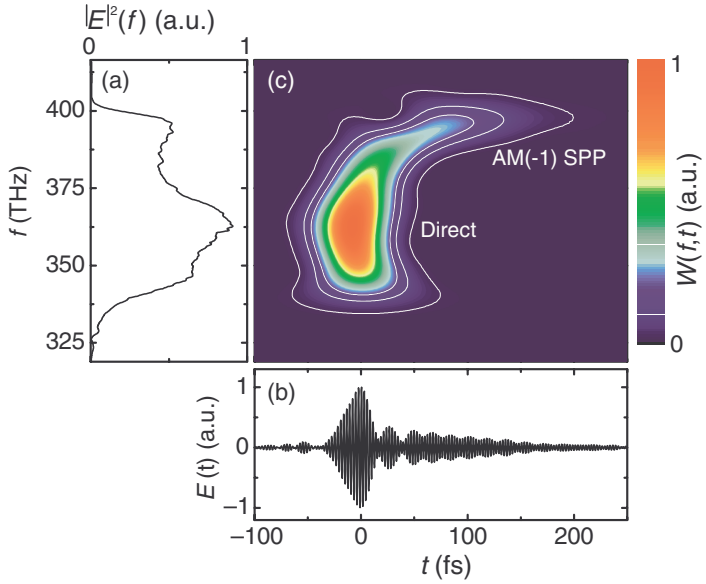

Figure 9. (a) Optical spectrum of the pulses transmitted through a 650 nm slit array at an angle of $\theta = 8^\circ$. (b) Pulse structure in the time domain. (c) Short-time Fourier transform showing that the transmitted pulse consists of an initial burst and a delayed long-lived SPP contribution.

transmitted field is well described by a nonresonant 'direct' transmission amplitude, E_{nr}, with a time structure given by that of the incident laser, and the damped emission from different SPP excitations at resonance frequencies ω_j and with damping constants Γ_j, namely

$$E_{\mathrm{out}} \propto E_{\mathrm{nr}} + \sum_j E_j \exp\left(-\mathrm{i}\omega_j t - \Gamma_j t\right). \tag{4}$$

In the spectral domain, the interference between the resonant and the nonresonant transmission channels gives rise to characteristic asymmetric line shapes, as predicted theoretically [45] and found on the basis of far-field transmission spectra [46]. Such line shapes [49] appear whenever a continuum is coupled to a resonance, for instance in the autoionization process in atomic physics [50]. Within this model, the complex transmissivity can be written as

$$t(\omega) = a_{\mathrm{nr}} + \sum_j \frac{a_j \mathrm{e}^{\mathrm{i}\phi_j}\Gamma_{\mathrm{rad},j}}{\omega - \omega_j + \mathrm{i}(\Gamma_{\mathrm{rad},j} + \gamma_j)}. \tag{5}$$

Here, a_{nr} is the spectrally flat or slowly varying nonresonant transmission amplitude, and a_j and ϕ_j are the oscillator strengths and phases, respectively. The frequencies ω_j correspond to SPP resonances at either the AM or SM interface [44]. The resonance width Γ_j contains two terms: a nonradiative damping γ_j due to absorption in the metal, and the radiative damping $\Gamma_{\mathrm{rad},j}$ of the SPP modes, which is in most cases dominant [16].

Figure 10 illustrates the physical picture underlying this line shape model and shows that the spectral dependence of both $T(\omega)$ and $\varphi(\omega)$ are satisfactorily reproduced. The model also shows that, as a consequence of the π-phase change across the Lorentzian SPP resonance, the resonant excitation of SPPs gives rise to an enhancement [14] of the transmission at certain

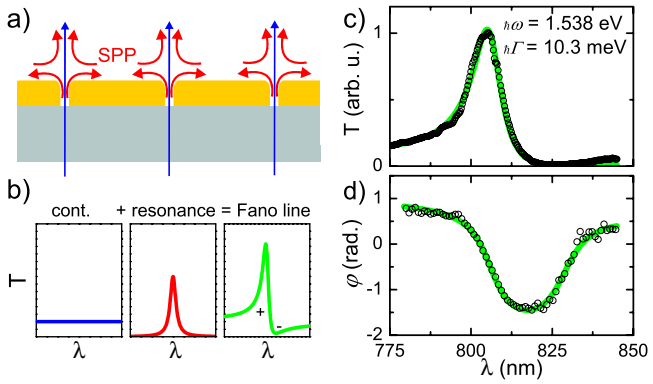

Figure 10. (a) Schematic representation of the resonant (red) and direct (blue) transmission components. (b) Illustration of a Fano-type resonance as the interference between a continuum and a resonant contribution, resulting in constructive (+) and destructive (−) interference of both components in the far-field. (c)–(d) Simultaneous fit of a Fano resonance (green lines) to the squared magnitude (c) and the spectral phase (d) of the measured complex transmissivity (open circles) at $\theta = 44^\circ$.

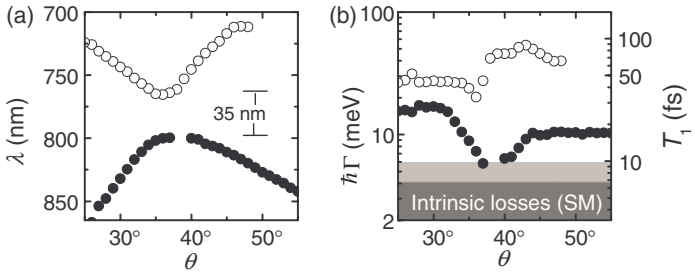

Figure 11. Formation of a plasmonic band gap for substrate-metal SPPs, evaluated from a fit to the Fano line shape. (a) Resonance wavelengths of the two branches. Two values are missing for the lower branch near $\theta = 38^\circ$ due to a disappearance of the peaks at these angles. (b) Linewidths and corresponding lifetimes of both branches (logarithmic scale). The upper borders of the light gray and gray shaded areas correspond to the expected intrinsic (absorptive) SPP damping for the dielectric function tabulated in [51, 52], respectively.

wavelengths, as well as to a transmission reduction [38] at other wavelengths, illustrated in figure 10(b).

This line shape model now forms a sound basis for a quantitative analysis of the effects of coherent SPP interactions, namely the formation of bandgaps on the transmission spectra of such nanoslit or -hole arrays. Coherent interactions are expected to become important whenever two or more SPP modes are brought into resonance. The essential consequences of such interactions are summarized in figure 11 for the crossing of the SM[+1] and SM[−2] modes of the nanoslit array with $a_0 = 650$ nm. For this array, $t(\omega, \theta)$ is recorded by SI with a step size $\Delta\theta = 1^\circ$ [42]. These data are analyzed using the line shape model described above (equation (5)), and the extracted resonance wavelengths $\lambda_j = 2\pi c/\omega_j$, widths Γ_j and SPP lifetimes $T_{1,j} = 1/(2\Gamma_j)$ are

shown in figures 11(a) and (b). One observes a clear anti-crossing of the two SPP branches near $\theta_c = 38^\circ$ and the formation of a plasmonic band gap with an energy $E_g = 72$ meV.

In addition to the splitting of the resonance frequencies, drastic intensity and linewidth variations are found. The linewidths of the upper and lower branches are plotted in figure 11(b) as the open and black circles, respectively. The most striking feature is the linewidth narrowing of the lower energy branch near the SM[1]/SM[−2] anti-crossing. Here, a minimum linewidth of $\Gamma \approx 5.5$ meV is found. This corresponds to a SPP lifetime of about $T_1 = 60$ fs, which is much closer to the intrinsic damping time than the lifetimes of the SPP resonances far from the anti-crossing, where shorter lifetimes down to a few femtoseconds are found. Thus, near the anti-crossing, the SPP lifetime is no longer limited by radiative damping [16] but by the intrinsic SPP losses. In addition, the intensity of the transmission decreases and eventually vanishes near the anti-crossing angle θ_c. This line-narrowing is evidence for a coupling-induced suppression of the radiative damping, i.e. a clear example of subradiance [53]. Near the anti-crossing, the type of SPP damping changes from predominantly radiative ($\Gamma_{rad} > \gamma$) to absorption-limited ($\gamma > \Gamma_{rad}$). For the case of the SM [+1]/SM[−2] crossing, these subradiance effects are somewhat masked due to the apparent asymmetry of the damping constants for $\theta < \theta_c$ and $\theta > \theta_c$ (figure 11(b)). This asymmetry arises because the SPP modes above the bandgap and with $\theta > \theta_c$ can couple into additional diffraction orders, resulting in an increase of radiative damping. The asymmetry is reduced near the AM [+1]/AM [−1] crossing and here, SPP lifetimes T_1 of up to 200 fs have been found for a grating with $a_0 = 750$ nm [42].

Spectrally-resolved near-field imaging of the optical modes in these plasmonic crystals (figure 12) is helpful in clarifying the cause of the damping suppression. For experimental reasons, such mode imaging is described at the crossing of the AM[+1] and AM[−1] modes. For such imaging, we illuminate the sample through the sapphire substrate near $\theta = 0^\circ$ with the broadband Ti : sapphire laser. The transmitted light is scattered off an Al-coated near-field fiber probe, dispersed in the far-field through a monochromator and detected with a CCD camera.

Figure 12(b) shows the spatially averaged near-field spectrum, normalized to the incident spectrum. The broad and the narrow resonances found in the far-field transmission forming the AM SPP bandgap are evident. In contrast to the corresponding far-field spectrum, the pronounced asymmetric line shape of the resonances has largely disappeared, since the relative magnitude of the nonresonant 'direct' transmission is greatly reduced in the near-field. Most important are the spatial near-field intensity distributions $I(x)$ along the surface at the wavelengths of the narrow (*dark*) and broad (*bright*) resonances (figure 12(c)). In the wavelength range of the broad resonance, $I(x)$ shows maxima at the slits and slightly weaker maxima in the center between slits. In contrast, at the wavelength of the narrow resonance, $I(x)$ shows almost negligible intensity at the slits and two strong maxima in-between the slits.

This suggests that these images reveal the optical mode profiles of the coupled SPP modes of these plasmonic crystals. In analogy to other periodic systems, e.g. in crystalline solids, the periodic structuring of the surface induces a coupling of the propagating SPP modes traveling to the left and right, resulting in new coupled normal modes. At normal incidence, the field distributions are expected to be symmetric and antisymmetric with respect to the slit centers, in agreement with the intensity distributions seen in figure 12(c). Since the nanoslits effectively serve as scattering centers, coupling evanescent SPP modes into propagating far field modes, it is apparent that the radiative damping of the dark mode is largely reduced. As the dark mode has a very small mode amplitude at the scattering centers, the coupling to far-field modes is reduced and the radiative damping vanishes strictly at normal incidence. This qualitative

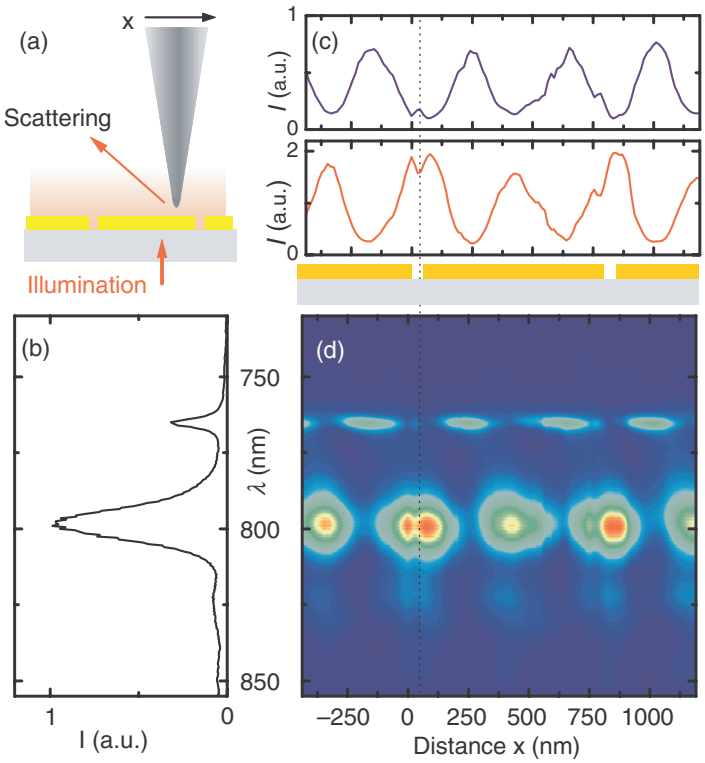

Figure 12. Near-field optical spectroscopic line scan of the AM bandgap ($a_0 =$ 750 nm), providing direct evidence for SPP Bloch modes. (a) Experimental configuration. An aluminium coated fiber tip is used to scatter the near fields into the far field. The scattered field intensity is recorded as a function of position and wavelength. (b) Spatially averaged near-field spectrum. (c) Spatial dependence of the near-field intensity at 766 nm (narrow resonance, blue curve, top) and at 800 nm (broad resonance, red curve, bottom). (d) Spatially and spectrally resolved near-field intensity as a function of the tip position along the x-axis, perpendicular to the slit axis, and as a function of the excitation wavelength λ.

explanation is confirmed by an analysis within a coupled mode model [42] and by quantitative scattering matrix simulations [40, 47, 48]. Due to the complex nature of the electromagnetic near-field in such nanostructures [54], one may expect that different polarization components of the electric field but also of the magnetic field are imaged in near-field experiments. More detailed experimental studies [48] show convincingly that the experimental geometry chosen here is most sensitive to the in-plane component of the magnetic field $H_y(x)$, oriented along the slit axis.

In summary, these experiments show that coherent optical spectroscopy using broadband laser sources in conjunction with spectrally resolved near-field mode imaging provides a very clear microscopic picture of the linear optical properties of such periodic metallic nanostructures and is the basis for a detailed theoretical description. We anticipate that similar experiments will be equally crucial in analyzing and optimizing the *nonlinear* optical properties of hybrid metal nanostructures, such as periodic metal/semiconductor or metal/polymer arrays, which promise new applications in nano-optoelectronics.

3.2. An isolated ultrafast light nanosource based on SHG at metallic nanotips

In the field of nano-optics there is a strong demand for nanometre-sized, isolated light emitters for enhanced resolution microscopy and spectroscopy, as well as for nanowriting applications. The most common approach for the production of such sources is the aperture NSOM probe, which confines the optical field to an evanescent, nonpropagating wave by a nanometre-sized aperture, usually realized by a metal-coated tapered optical fiber [31] or a metal-coated cantilevered hollow pyramid with a hole at its apex [55]. Although the spatial resolution of such probes can in principle go down to 20 nm, determined by the skin depth of the metal coating, it is for conventional probes often limited to 50–100 nm by the low throughput (typically around 10^{-4}–10^{-5}) along with the low value of the average input power (a few milliwatts) that can be coupled before the onset of thermal probe damage [56]. Recently, more sophisticated aperture probe concepts, such as the double-tapered fiber [57] or the tip-on-aperture probe [58]–[60], have been introduced that overcome these limitations to a certain extent.

An interesting alternative approach to dramatically improve the lateral resolution to the 10 nm range is the s-NSOM, in which sharp AFM tips with apical radii down to 2 nm are used as near-field scatterers [61]. Field enhancement at the tip apex allows the achievement of 5–10 nm resolution [20], [62]–[64] with either metallic or semiconducting tips. On the other hand, s-NSOM is generally affected by a strong global background coming from the far-field illumination. This background exceeds the local signal coming from the nanometric scatterer by several orders of magnitude and severely limits the applicability of the s-NSOM approach. Special tip–sample distance modulation techniques, together with homodyne or heterodyne interferometric set-ups for signal enhancement, are in fact required to extract the desired near-field signal from the background [62]–[64]. Several approaches have been undertaken to reject this large background, e.g. (i) the use of a total internal reflection (TIR) configuration [20, 65], where the tip is illuminated by the evanescent field created at the surface of the substrate by TIR; (ii) optical pumping of a fluorescent nanometre-sized emitter at the tip apex, such as a single molecule [66], that allows spectral filtering of the background radiation; (iii) the use of the tip enhancement to excite a nonlinear optical process in the material, such as two-photon fluorescence [67] or Raman scattering [68, 69]; or (iv) a nonlocal tip illumination by coupling the incident light to surface polaritons [70].

Here, we propose an s-NSOM configuration based on the detection of the SH radiation induced at the tip apex upon illumination with high peak power ultrashort light pulses [71]. SHG at a metal tip results from a combination of field enhancement due to an electrostatic ‘lightning rod’ effect, induced by the tip sharpness, and the excitation of localized surface plasmon resonances. The electric field of the incident light interacts with the free electrons in the metal, leading to charge accumulation at its surface; when the polarization is parallel to the tip axis, the charge density, and thus the electric field, are localized at the tip end [37, 67]. Since the SH emission efficiency depends quadratically on the incident intensity, it should be strongly confined at the tip apex, thus providing an isolated nanosource of short light pulses which can be used for illuminating a sample brought into its near-field. Provided that the intensity of local tip-enhanced SH emission is sufficiently high, this configuration has the advantage of greatly increasing the signal-to-noise ratio since the background elastic scattering at the fundamental wavelength (FW) is filtered out due to the local enhancement of the optical nonlinearity at the tip apex.

SHG from sharp metal tips has been reported both for illumination with picosecond [72, 73] and femtosecond [74, 75] pulses. Typical values of the SH signal obtained in previous

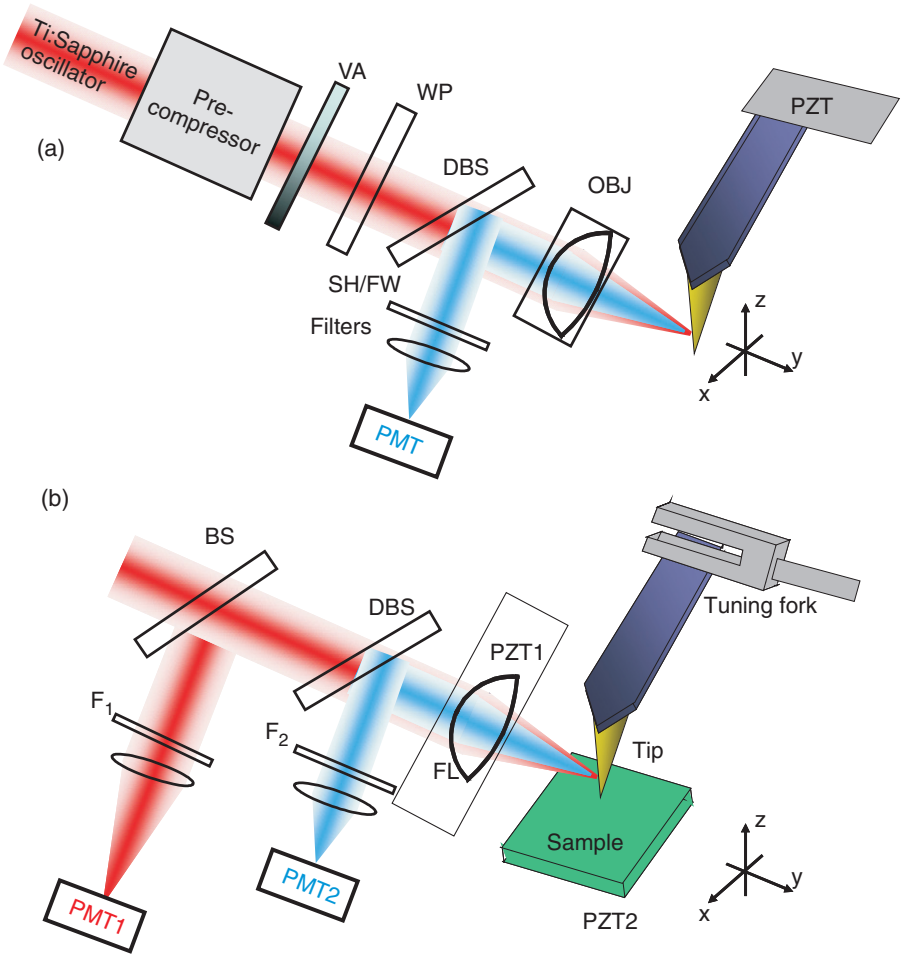

Figure 13. (a) Experimental set-up used for characterizing SH emission from the AFM tips. VA: variable attenuator; WP: $\lambda/2$ waveplate; DBS: dichroic beam splitter; OBJ: microscope objective; PZT: piezoelectric scanner; PMT: photomultiplier. (b) Experimental set-up of the SH s-NSOM. BS, beam splitter; FL, focusing lens; F, filters. Proportions of cantilever, tuning fork and tip are exaggerated.

experiments are in the range of 10^3–10^4 photons s^{-1}. Our system introduces a novel and much more efficient illumination and light collection apparatus, utilizing high peak intensity femtosecond pulses from a stretched cavity Ti : sapphire laser. In this way, the number of detected photons at the SH wavelength can be increased by several orders of magnitude (up to 10^6–10^8 photons s^{-1}), thus opening up new and realistic applications for this nanometre-sized optical source for microscopy and spectroscopy.

We first characterized the far-field emission from the tip using the experimental set-up shown in figure 13(a) in order to demonstrate that the SHG is strongly localized at its apex and that the tip acts as a nonlinear nanoantenna oriented along its axis. We adopted a grazing incidence illumination and collection configuration, with the tip nearly perpendicular to the beam propagation direction. This configuration has the advantage of exciting the tip dipole along its axis and collecting the nonlinear scattered light along the direction of maximum emission.

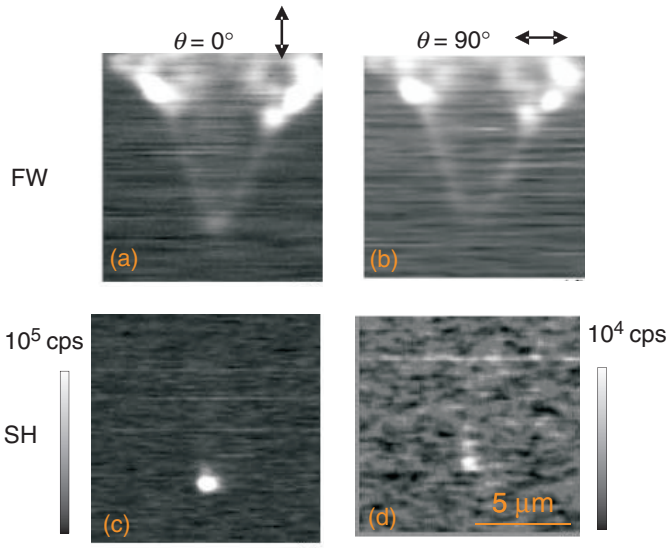

Figure 14. FW (a, b) and SH (c, d) maps of the tip scattering as a function of the illumination position, for polarization parallel (a), (c) or perpendicular (b), (d) to the tip axis. In these images, the tip is moved into the beam waist of the laser focus and raster-scanned within the x–z-plane. The tip axis is oriented along z.

Note that, though less critical than with aperture probes, thermal damage can affect irradiated AFM tips if the average power density exceeds $\sim$1 MW cm^{-2} [76]. This problem is alleviated by the use of our stretched-cavity oscillator, which reduces the average power for a given peak power level (see section 2.1). The femtosecond pulse train is first sent to a prism pair pre-compressor that compensates for the pulse broadening arising from the optical components in the beam path from the laser to the tip. To focus the laser beam on the AFM tip with a very narrow spot size, a 63×, 0.85 N.A. microscope objective is used. The laser is modulated by a mechanical chopper at a frequency of 1 kHz. The back-scattered light is collected by the same illumination objective and directed by a dichroic beam splitter towards a UV-extended PMT. To further filter out the FW beam, short-pass filters and a broad-band interference filter centered at 400 nm and with a 40 nm passband are used. The PMT current is fed to a low-noise transimpedance amplifier and then to a lock-in amplifier referenced to the modulation frequency. The residual FW beam reflected by the dichroic beamsplitter can be detected by a PMT with red-extended sensitivity by replacing the filter set described above by a single long-pass filter.

To characterize the behavior of the metal tip as a localized SH source, we have fixed the AFM sensor chip, mounting a cantilever to which the tip is attached on the x–y–z-piezoelectric stage normally used for sample scanning. The 15 μm long tips used in the experiments are made of Si and are coated with a 20 nm thin layer of PtIr or gold. Scans of the tip position through the laser focus are accomplished by a raster motion in the (x–z)-plane (see figure 13(a)). The tip axis, z, is rotated by about 20° with respect to the focal plane, in order to avoid possible shadowing of the highly focused illumination beam by the cantilever apex.

Figure 14 shows pictures of a lateral (x–z) scan of the laser spot at the FW and SH wavelengths, respectively, with different polarizations of the FW beam. The y-coordinate is held fixed at the beam waist position. The appearance of the AFM pyramidal tip is clear in the FW image shown in figure 14(a). Note that the pyramid borders and the tip apex

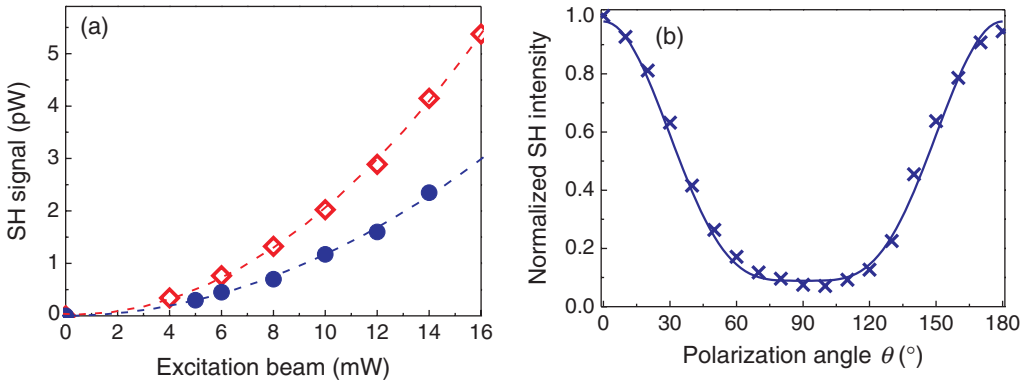

Figure 15. (a) Average SH power versus FW power incident on the tip, for polarization parallel to the tip axis and for gold (diamonds) and PtIr (circles) tips. (b) Plot of the SH power versus the angle θ between the electric field polarization and the tip axis, along with a superimposed $\cos^4\theta$ fitting (solid line).

exhibit approximately the same amount of enhanced scattering. For an excitation polarization orthogonal to the tip axis (figure 14(b)), the apex contribution sizably decreases, in agreement with the previous discussion. This picture highlights the strong background due to global illumination arising in s-NSOM at the FW. Figures 14(c) and (d) show the corresponding images at the SH wavelength. In contrast to figures 14(a) and (b), field enhancement at the tip apex provides a clearly isolated light source exclusively at the tip location. The field enhancement and the SHG efficiency are much higher for a polarization parallel to the tip axis (figure 14(c)) than for perpendicular polarization (figure 14(d)).

The second-order character of the tip-enhanced nonlinearity has been assessed by input–output characteristic curves (figure 15(a)), yielding quadratic behavior for various polarizations, collection geometries and tip metals. The efficiency of the gold tips was typically 2–3 times higher than the PtIr ones, but the latter were preferred due to the far higher mechanical robustness, more suitable for near-field microscopy applications. With 1.5 mW of incident average power, corresponding to an illumination power density of 0.1 MW cm^{-2}, the collected power from the PtIr tips amounts to 0.5 pW. This value corresponds to about 10^6 photons s^{-2}, which is about 2–3 orders of magnitude higher than values obtained in previous experiments performed with gold tips. Taking into account the collection losses of our system (transmitted power at the SH wavelength about 20%), we obtain a throughput of about 2×10^{-6} by considering only the SH radiated within our collection solid angle. An increase of the laser power up to the safety threshold for thermal damage could raise this figure by two orders of magnitude. Figure 15(b) shows the measured dependence of the SHG on the incident polarization direction (crosses). In the same figure, a fit using a $\cos^4\theta$ function, where θ is the angle between the tip axis and the laser polarization direction, is also shown as a continuous line. This line is seen to fit very well with the experimental data. This shows that the SH signal is mainly induced by the component of the incident electric field vector which is oriented along the tip axis and strongly enhanced at the tip apex. This finding is in agreement with previous model calculations [67] and experiments [77]. A more detailed study of the polarization properties of the SHG from sharp metal tapers has recently been reported in [75].

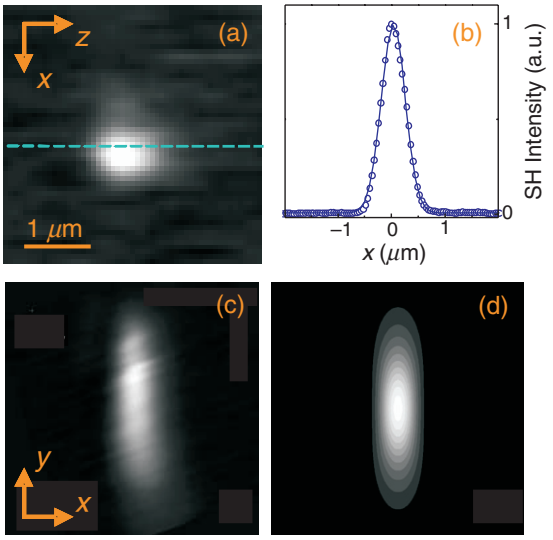

Figure 16. (a) x–z map of the SH emission of the tip for polarization parallel to its axis and (b) cross-sectional profiles along the z-direction (diamonds) together with a Gaussian fit (solid lines). (c) x–y map of the SH emission of the tip for polarization parallel to its axis and (d) calculated SH intensity of a Gaussian beam along the beam propagation direction.

Figure 16 shows an expanded view of an x–z scan (a), together with a cross-section (b). Here, the image resolution is limited by the laser spot size. The real size of the nanosource is expected to be much smaller than the wavelength and needs to be assessed by near-field characterization. Figure 16(c) shows an experimental SHG map as obtained upon scanning the tip in the y–z-plane, where y is the propagation direction of the optical beam. For comparison, figure 16(d) shows the theoretical image obtained from the theory of Gaussian beam propagation, plotting the SH intensity of a beam with a 550 nm spot size at the beam waist. The good agreement between experiment and model demonstrates further that the light is emitted by a confined source with a size much smaller than the laser spot size.

In order to use the SH nanosource for microscopy, it is necessary that the tip is approached to the sample. The set-up of the SH s-NSOM is shown in figure 13(b) and is essentially a home-made AFM (described in section 2.2) modified in order to allow for optical access in illumination and collection. To permit the sample approach with negligible shadowing of the tip illumination, we replaced the 63× microscope objective by an aspheric lens with 6 mm working distance. The generated SH is detected by a UV-extended PMT (PMT2 in figure 13(b)). Back-scattered light at the FW is detected by an additional red-enhanced PMT (PMT1 in figure 13(b)). In this way, apertureless images at the FW and SH wavelengths can be recorded simultaneously and directly compared. To improve the signal-to-noise ratio in detection, we use an optical chopper in combination with a lock-in amplifier, operating at a frequency of 2.2 kHz in order to not induce periodic tip deformations due to thermal effects that may occur with characteristic times longer than 1 ms.

To optimize the image contrast, proper alignment of the laser spot is necessary so as to favor the tip SH emission in comparison to the global SHG from the sample. To this purpose the aspheric lens is mounted on an x–y–z piezotranslator (Nanocube, Physik Instrumente,

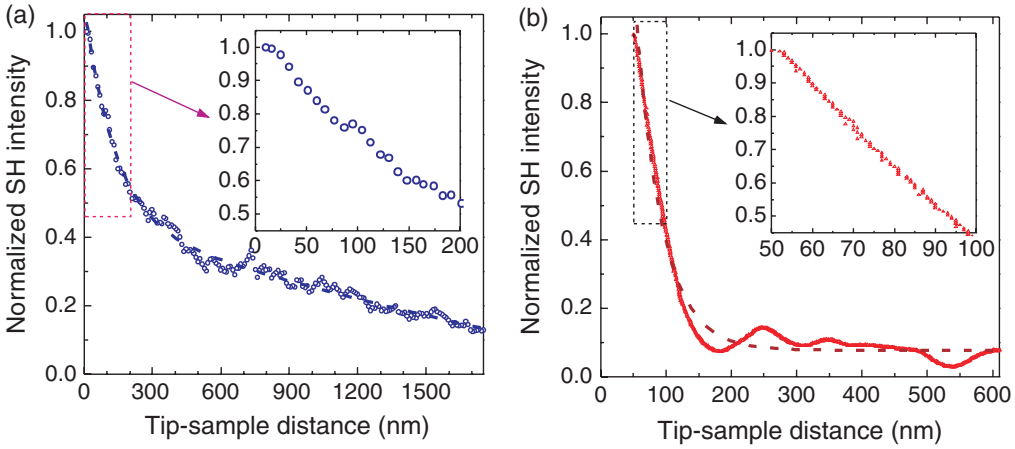

Figure 17. SH approach curves in (a) the non-modulated case and (b) with tip/sample distance demodulation.

Germany). An indication of proper alignment can be given by SH approach curves, i.e. plots of SH intensity as a function of tip/sample distance. An example of such a curve, obtained by approaching the tip to a gold sample, is shown in figure 17(a). The curve is fitted by a double exponential function, indicating the existence of two distinct regimes. At large distances ($\gg \lambda$) there is a gradual increase of SH. This signal is assigned to the nonlinear response of the sample, since the emission rises within a distance comparable to the Rayleigh range of the illumination beam. Such an increase is therefore due to the fact that the sample is brought into the focal region of the illumination spot and thus emits SH more efficiently. At short distance ($< \lambda/2$), a steeper increase is recorded. This is assigned to the near-field contribution to the SH signal.

To further suppress the far-field contribution, one can use a periodic probe/sample distance modulation, a common method in s-NSOM experiments to reject global contributions to the optical signal [62]–[64]. This background suppression is shown by the approach curve in figure 17(b), in which we remove the optical chopper and reference our lock-in amplifier to the actual tip oscillation. The used integration times in this experiment are much higher than in the previous case (1 s versus 100 ms) and are limited by the SH signal intensity. The difference between this curve and the one recorded without modulation is the absence of long-range contributions, as well as the much steeper short-range increase of the SH signal. The use of tip/sample distance modulation techniques is well known to suppress both background contribution and topography artifacts in standard s-NSOM, although resorting to higher harmonic demodulation is necessary in that case, since first-order demodulation is dominated by topographic artifacts [62, 63]. Here, on the contrary, first-order demodulation is not affected by similar drawbacks.

Figure 18 shows a first SH s-NSOM image of a test sample consisting of gold triangles (height 15–25 nm) on a glass substrate obtained from a projection pattern ('Fischer pattern' [78]) in a hexagonal array with 453 nm periodicity. The characteristic hexagonal structure of this sample is clear from the topographic image in figure 18(a). The corresponding SH image is shown in figure 18(b). In this case, the total SH signal was recorded without tip–sample distance demodulation. In contrast, the FW image (not shown) is nearly independent of the tip

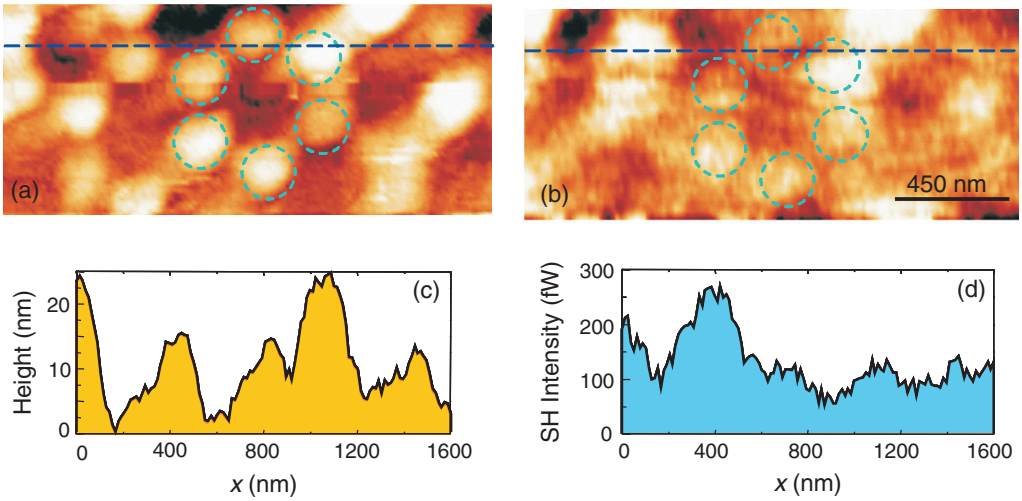

Figure 18. (a) Topographic image of a Fischer pattern, and (b) simultaneously acquired SH s-NSOM image. Line profiles extracted from (c) the topographic image and (d) from the SH image.

position, as expected for a non-modulated s-NSOM image with amplitude detection. The FW image is essentially fully dominated by the global background. Line profiles in figure 18(c) and (d) evidence that: (i) even without demodulation the contrast of the optical image is quite high, exceeding 100% and (ii) the SH s-NSOM image differs quite significantly from the topographic image. This is demonstrated by finding structures in the topography that have almost no corresponding SH signal, and by observing that the SH intensity of the different triangles does not correlate with their topographic height. From such images, however, it is difficult to fully rule out topography effects on the image. This can be achieved, however, by recording local SH approach curves. The contrast achieved on similar samples with aluminium triangles did not exceed 20%; therefore there are indications that this technique is able to discriminate different metals. More detailed studies are underway to investigate how the local SH intensity in s-NSOM is correlated to the local optical nonlinearity of the sample.

These preliminary results indicate the possibility of using the SH s-NSOM technique to achieve background-free imaging of nanostructured surfaces with very high spatial resolution. However, several improvements remain to be made. First of all, the SHG efficiency at the tip can be increased by further reducing the pulse repetition rate to the 1–2 MHz range using an acousto-optic pulse picker. In this way, the energy and the peak power of a single pulse are increased for a given safe average power level. In addition, figure 17(b) highlights the advantage of using tip–sample distance demodulation to suppress the SH background; this approach is, however, made difficult by the low SH signal levels, so that only a few photons per oscillation cycle are detected. The SH sensitivity could be boosted by a homodyne set-up, in which the SH generated by the tip is made to interfere with a strong SH signal generated in the far-field by a standard nonlinear optical crystal.

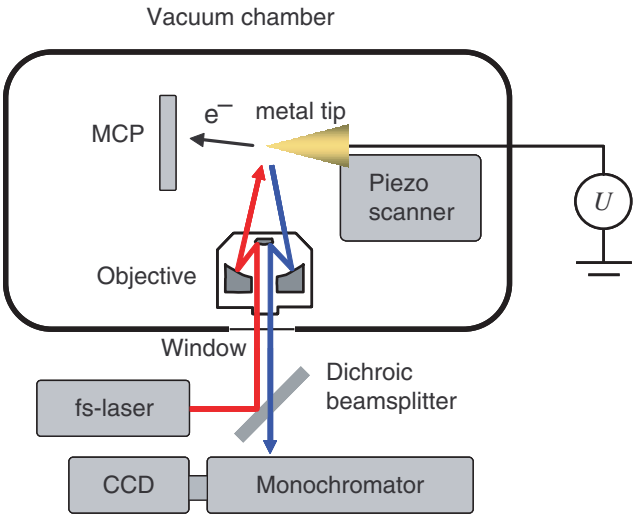

Figure 19. Experimental set-up for the simultaneous detection of electron emission and nonlinear light generation from ultrasharp metal tips. Optical pulses from a fs-laser are focused with a Cassegrain mirror objective on to the tip. Both objective and tip are mounted inside a vacuum chamber and the optical pulses are coupled into this chamber through a thin quartz window. The emitted electrons are detected with an MCP. An arbitrary bias voltage U can be applied to the tip.

3.3. A nanometre-sized femtosecond electron source based on optical field enhancement at metallic nanotips

The efficient generation of SH radiation from single metal nanotips reported in section 3.2 leads us to the exploration of other, higher order nonlinear processes from such tips. A particularly interesting example is the field-induced generation of ultrashort electron pulses via a local photoelectric effect induced by multiphoton absorption [79, 80] or by optical field emission [81, 82]. Here, the field enhancement at the very end of the metal tip may greatly lower the required field strengths for observing such phenomena [83, 84]. Hence, bright and spatially localized electron sources may be obtained at the fairly moderate peak powers achievable with high repetition rate laser sources. Such sources should find important applications in ultrafast electron diffraction [85]–[87] and microscopy [88, 89], fascinating new approaches to the study of microscopic structural dynamics with picosecond or even sub-picosecond temporal resolution.

To investigate electron generation from sharp metal tips, we have developed the experimental set-up sketched in figure 19 [84]. Seven-femtosecond light pulses from a Ti : sapphire laser are coupled via a 150 μm thick quartz window into a high vacuum chamber and are then focused to a spot size of about 1.5 μm by a reflective Cassegrain microscope objective (numerical aperture 0.4, working distance 10 mm). An eletrochemically etched gold tip with a radius of curvature of about 20 nm is mounted on a hardware-linearized piezo scanner and can be raster-scanned through the laser focus. For electron detection, a chevron-type micro-channel-plate (MCP) detector is placed opposite to the tip, and voltage pulses from the MCP detector resulting from single electron events are counted with an electronic discriminator.

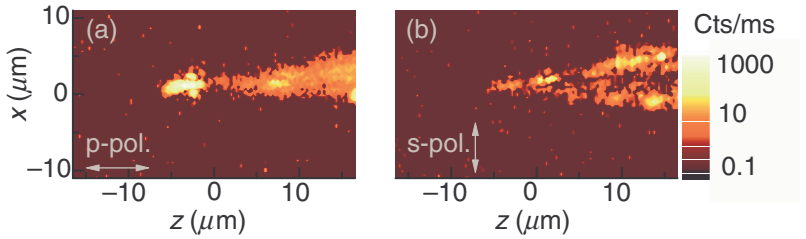

Figure 20. Electron generation rate (logarithmic color scale) for an incident polarization parallel (a) and perpendicular (b) to the tip axis oriented along z. For perpendicular polarization, the electron emission from the tip apex is suppressed by more than two orders of magnitude.

A variable bias voltage U can be applied to the tip. In addition, backscattered light from the tip is collected via the Cassegrain objective, separated from the incoming laser by a dichroic beam splitter, dispersed in a monochromator and detected with a liquid-nitrogen-cooled CCD.

We first study the spatial characteristics of the electron generation by probing the electron signal while scanning the tip in the plane perpendicular to the optical axis (y-direction) through the laser focus (figure 20). In these images, the electron signal is plotted on a logarithmic intensity scale. When the polarization direction of the incident laser is oriented along the axis of the metal tip (y-direction), we observe, at $U = 0$, an intense electron signal ($>10^6\,\mathrm{e}^-\,\mathrm{s}^{-1}$) from a $0.5 \times 1\,\mu\mathrm{m}^2$ region at the very end of the metal tip. This spot size is smaller than the illuminating spot size of $1 \times 2\,\mu\mathrm{m}^2$, assessed by analyzing the simultaneously recorded backscattered laser light. The geometry of the electron emission spot is not fully elliptical, small side lobes along the x-axis reflect the imperfect shape of the laser focus generated by the Cassegrain objective. In this image, a much weaker electron signal is also observed on the tip shaft. When rotating the incident polarization to the perpendicular direction, the emission from the tip apex is reduced by more than two orders of magnitude, clearly illustrating the polarization selectivity of the field enhancement promoting the electron generation. In addition, the image shape of the weak shaft signal changes. For parallel polarization, this background signal stems from the front face of the tip shaft, whereas the emission for perpendicular polarization is mostly arising from the borders of the tip shape. This is understood by considering that this background is preferentially occurring from micro-roughness spots at which the incident electric field is pointing away from the surface. We finally note that, similar to the results described in section 3.2, we also observe rather intense SHG and two-photon induced photoluminescence [74, 77] at the tip apex at exactly the same spot at which the electron signal for parallel incident polarization has its maximum [84]. Evidently, also this local SH signal shows a pronounced polarization dependence similar to that shown in figure 15 [75].

We now want to investigate the physical mechanism underlying this field-enhanced electron generation in more detail. For this purpose, we move the metal tip directly into the laser focus and study the intensity and tip bias voltage dependence of the electron signal. In order to evaluate these experiments, it is important to remember that, in the absence of optical fields, electron emission from metal tips occurs at sufficiently high negative static bias voltages due to Fowler–Nordheim tunneling [90]. If the resulting surface electric field reaches a few $\mathrm{V\,nm}^{-1}$, quantum mechanical tunneling of electrons from filled states near the Fermi energy becomes possible. Within the WKB approximation [91], the transmission coefficient of an electron of

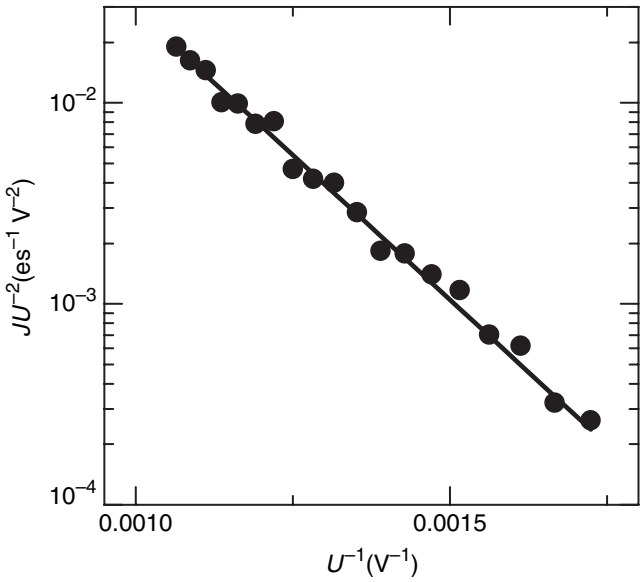

Figure 21. Fowler–Nordheim plot of the tunnel emission of a gold tip (circles) and a fit to a FN dependence (line).

energy E through the triangular barrier of height $\Phi - E$ created by a surface electric field F is [90]

$$T(E) = \exp\left(-\frac{4\sqrt{2m}(\Phi - E)^{3/2}}{3\hbar eF}\right). \tag{6}$$

In equation (6), the original Fermi energy is set to zero, so that the work function Φ is used as a parameter. This function can be integrated over the filled density of states of the metal, yielding the tunnel current density j. If image charge effects of the tunneling electrons are taken into account [90], j is expressed as

$$j = \frac{e^3F^2}{16\pi^2\hbar\Phi t^2(y)} \exp\left(\frac{-4\sqrt{2m}\Phi^{3/2}v(y)}{3\hbar eF}\right). \tag{7}$$

Here, v and t are elliptical dimensionless Nordheim functions of the variable $y = e^{3/2}\sqrt{F/4\pi\epsilon_0}/\Phi$ (see [90] and corrected expressions in [92]). $t^2(y)$ is a slowly varying function often set to a value of 1.1, and $v(y)$ is frequently approximated as $v(y) = 0.95$–y^2 [93, 94]. The overall tunneling current J then is the surface integral over the current density j. Such a model correctly describes the tunneling emission from our gold tips in the presence of a static bias voltage (figure 21). In particular, it allows us to calibrate the proportionality constant between a macroscopically applied bias voltage U and the resulting surface electric field F. From the slope of the data, a surface electric field of $F \approx 10^{-2}\,\mathrm{nm}^{-1}U$ is deduced.

After this initial characterization, the electron flux J is studied systematically as a function of the incident laser power P and the tip bias voltage U. Figure 22 shows a data matrix $J(U, P)$ (a), together with curves at constant incident power (b) and constant voltage (c). First, the power dependence for different voltages (figure 22(c)) is discussed. By evaluating the slope of this double-logarithmic plot, log J versus log P, one finds a clear fourth-order power dependence

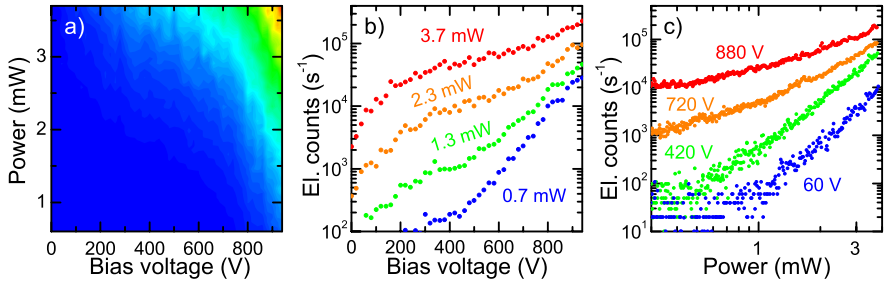

Figure 22. (a) Power- and voltage-dependent electron emission. (b) Voltage dependent curves at four different incident powers. (c) Power-dependent curves at four different bias voltages.

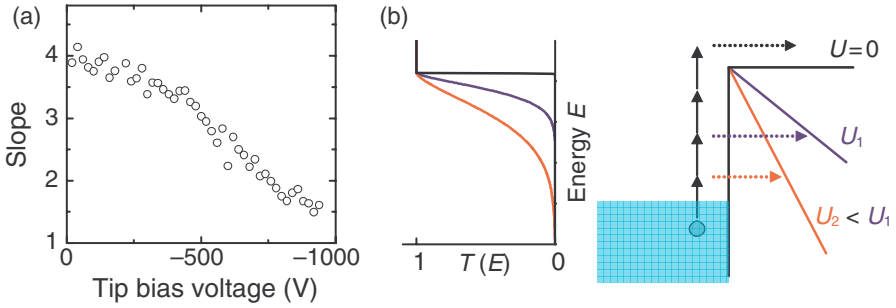

Figure 23. Slope of the double-logarithmic power dependence as a function of bias voltage. (b) Illustration of the bias-voltage-induced reduction of the effective nonlinear order. Applying a bias voltage from zero (black) over moderate (blue) to high (red) magnitudes, lower excited states increasingly contribute to the emission.

at low bias of less than 150 V. This steep slope shows that multiphoton absorption causes the electron emission at low bias voltage. Raising the bias voltage to higher negative values results in a background due to the static FN tunneling, and, most importantly, in a decrease of the power dependence of the emission. At $U = 880$ V, the electron flux is only slightly nonlinear with a power dependence $\propto P^{1.5\pm0.1}$ around $P = 3$ mW. The gradual decrease of the power dependence, evaluated for the slope of the curves around 3 mW after subtraction of the dc contribution, is plotted in figure 23(a). The curve starts at a value of 4 with convex curvature, has an inflection point near 500 V and approaches 1 for larger bias voltages. In figure 23(b), an explanatory tunneling scheme is depicted, together with the WKB tunneling probability T as a function of electron energy for moderate (blue) and large (red) magnitudes of the bias voltage. For zero bias, only electrons excited by multiphoton absorption to states above the vacuum level can escape the metal. At high bias, multiphoton electron emission is complemented by tunneling from lower-lying electron states which may be excited by linear absorption processes. With increasing negative bias, the electron emission thus becomes dominated by photo-induced tunneling from electron states below the vacuum level.

Due to the rapid electron dephasing and relaxation processes in metals [95], finding a direct relation between a given power dependence and the relative contributions from

linear and multiphoton absorption processes is nontrivial. In principle, such an assignment requires a full dynamical simulation of the nonequilibrium dynamics of the highly excited electron system within the confined tip geometry, including the coherent excitations of the electron and many-body correlations. To our knowledge, there is limited information on these intricate nonequilibrium electron dynamics in nanostructures. We thus use a different, more phenomenological approach to learn about the nonequilibrium excitations of the electron system that give rise to the electron emission. The approach relies on an extension of the conventional Fowler–Nordheim approach, which assumes that $J(U, P)$ is given by an integral over the energy- and voltage-dependent transmission coefficients $T(E, U)$ times a distribution function of the optically excited carriers $f(E, P)$:

$$J(U, P) \propto \int_0^\infty \mathrm{d}E\, T(E, U)\, f(E, P). \tag{8}$$

The emission probability $T(E, U)$ of a state at energy E for a bias voltage U is assumed to be the same as for the conventional static FN tunneling in figure 21. The knowledge of $T(E, U)$ then permits a reconstruction of the carrier distribution $f(E, P)$ from the measured functional dependence $J(U, P)$. The desired function $f(E, P)$ is a time average over the transient nonequilibrium electron distribution during the course of the emission process. No implicit assumptions about the density of states are made, so that $f(E, P)$ describes the absolute carrier densities.

To obtain a numerical estimate of $f(E, P)$, equation (8) is discretized and rewritten as a matrix equation. The variable U is written as a vector with components U_i, $i \in \{0, 1, \ldots, 50\}$ denoting the voltages $U_i = i \cdot 20\,\mathrm{V}$ from 0 to 1000 V, at which the electron emission is measured. The carrier distribution function $f(E, P)$ is discretized in energy with a step size of 500 meV.

More specifically, we write

$$f(E, P) = \sum_j \frac{g(E_j, P)}{\mathrm{e}^{-E-E_j/\Delta E} + 1}, \tag{9}$$

where $g(E_j, P)$ is the coefficient of the carrier density in the interval between E_{j-1} and E_j. This transformation yields a matrix for the resulting tunneling current at the voltage U_i for each of these j components via

$$S(E_j, U_i) = \int_0^\infty \mathrm{d}E \frac{1}{\mathrm{e}^{-E-E_j/\Delta E} + 1} T(E, U_j). \tag{10}$$

With these definitions, the desired matrix equation can be expressed as

$$J(U_i, P) = \sum_j S(E_j, U_i) g(E_j, P). \tag{11}$$

Least squares solutions for $g(E, P)$ are calculated numerically by minimizing the error functional

$$\varepsilon = \sum_i |J(U_i, P) - \sum_j S(E_j, U_i) g(E_j, P)|^2 \tag{12}$$

for every incident power. The minimization is performed under the further constraint of non-negativity of the components of g. Consequently, only monotonically decreasing distribution functions are captured, excluding a strong resonant behavior at specific energies. The experimental data can be satisfactorily described by this class of distribution functions. From

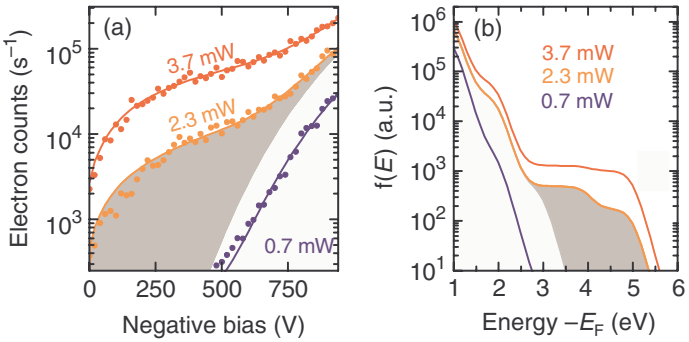

Figure 24. Voltage-dependent emission curves (dots) and the currents (lines) predicted from the reconstructed carrier densities shown in (b).

the optimized coefficients g, the corresponding distribution functions are calculated via equation (10). Figure 24(a) shows again the voltage-dependent emission curves at three incident powers (circles). The reconstructed distribution functions are shown in figure 24(b) for these three incident powers. As a consistency check, the solid lines in figure 24(a) represent the electron currents (equation (11)) resulting from these three distribution functions, which are in excellent agreement with the experimental results. The particular choice of the energy step size $E_j - E_{j-1}$ and the width of the Fermi functions ΔE (0.3 eV in figure 24) has proven to be of minor importance, and very similar results are obtained for a finer energy resolution.

The distribution functions possess, in particular for high optical powers, a markedly nonthermal character and are mainly composed of two components: (i) a strong low-energy component close to the Fermi energy likely to originate predominately from single-photon absorption; its energy content scales approximately linearly with the incident optical power. (ii) A nonthermal high energy shoulder which emerges between 3 and 6 eV (indicated by the gray-shaded area in figure 24(b) for $P = 2.3$ mW) with a strong nonlinear power dependence, resulting from multiphoton absorption from states below and up to the Fermi energy. It is this second component in the distribution functions which is responsible for the emission at low bias voltages, as is illustrated by the large gray-shaded area in figure 24(a) that corresponds to emission from the shaded area in the distribution function in figure 24(b). Although a substantial electron emission is already present at zero bias voltage, there is a sharp rise in electron flux upon increasing the bias from 0 to 100 V. This fact suggests that the major fraction of the nonthermal component populates states somewhat below the vacuum level.

The strong nonthermal character of the electron distributions has direct consequences for the time structure of the emitted electrons. For low voltages, the rapid thermalization of electrons limits the population lifetime of the relevant high-energy states [95, 96] and, thus, the duration of the emitted electron pulses. For very large negative bias, lower-lying states of longer lifetime [97] contribute significantly to the emission, possibly resulting in longer electron pulses.

Recent experiments [83, 98] suggest that Keldysh-type [81, 83] optical field emission from the states near the Fermi energy may be important because of the high electric fields of the excitation pulses. In our experiments, despite the short laser pulses and the substantial field enhancement at the metal tip, we estimate a Keldysh parameter of about 4 at $P = 3$ mW. We thus expect that the present experiments are well within the multiphoton regime [99], although at this

stage, a limited contribution of optical field emission cannot be fully be ruled out at the highest bias voltages. At lower bias voltages, the situation is clear, as we find the same fourth-order power dependence for various tips at zero bias, whereas optical field emission should strongly depend on the local field enhancement and thus vary from tip to tip. Furthermore, for optical field emission, a saturation of the power dependence to a finite value (4 in our case, cf figure 23) is not expected at zero bias. Instead, optical field emission predicts a steeply increasing power dependence for a reduction of the bias [98].

4. Summary

The results presented in the previous sections describe some of the progress made in the laboratories of the authors in combining ultrafast spectroscopy and nano-optical imaging techniques.

The linear optical properties of metallic nanostructures such as plasmonic crystals are now much better understood, partly due to the new information gained by combining temporally and spatially-resolved spectroscopy. In particular, periodic nanohole and nanoslit arrays have developed into important model structures for studying the optical properties of plasmonic crystals. This improved knowledge may be crucial for exploring the nonlinear optical properties of new hybrid structures consisting of metals and optical gain media, e.g. metal/semiconductor or metal/polymer complexes, where new phenomena such as SPP amplification or lasing are expected.

The field localization at metallic nanostructures gives rise to spatially highly localized optical nonlinear effects. A prominent example is SHG from metal nanotips which allows one to create nanometre-sized isolated light spots with dimensions down to the 10 nm range. The use of optimized ultrafast laser designs has been shown to greatly enhance the efficiency of these nonlinearites and thus the brightness of these nanolights. This opens the door for various new applications in nanoimaging and spectroscopy. A specific example is the imaging of nanometre-sized domains in polymer [100] or magnetic materials.

The results in section 3.3 show that this field localization is sufficiently strong to not only induce SHG but also the emission of an intense beam of electrons. This electron emission is localized to a nanometre-sized region at the apex of sharp metal tips [84]. Even though the time structure of the emitted electron burst has not yet been fully characterized, our experiments indicate that in the absence of a bias voltage, where electrons are emitted from energy states close to the vacuum level, the pulse duration is of the same order as that of the incident sub-10 fs light pulses and can possibly be reduced even further. Various applications can be foreseen for such a nanometre-sized femtosecond electron source. It will be interesting to test it as a source for ultrafast electron diffraction experiments [85, 86, 101]. At present, the time resolution in such experiments is limited to several hundreds of femtoseconds, partly due to the Coulomb repulsion of electron bunches produced at kHz repetition rates. In the field-enhanced emission from metal nanotips, high repetition laser sources are used, creating mostly only a single electron per pulse. Temporal smearing due to Coulomb repulsion can thus be avoided, possibly resulting in an increased temporal resolution. Also the small spot size of the electron source should be beneficial, since the temporal smearing due to spatial propagation effects may be reduced. Another interesting application of such electron sources is their use in tip-enhanced electron microscopy. The concept of such an electron microscope, based essentially on the modification of the ultrafast local electric field inducing the electron emission, is schematically

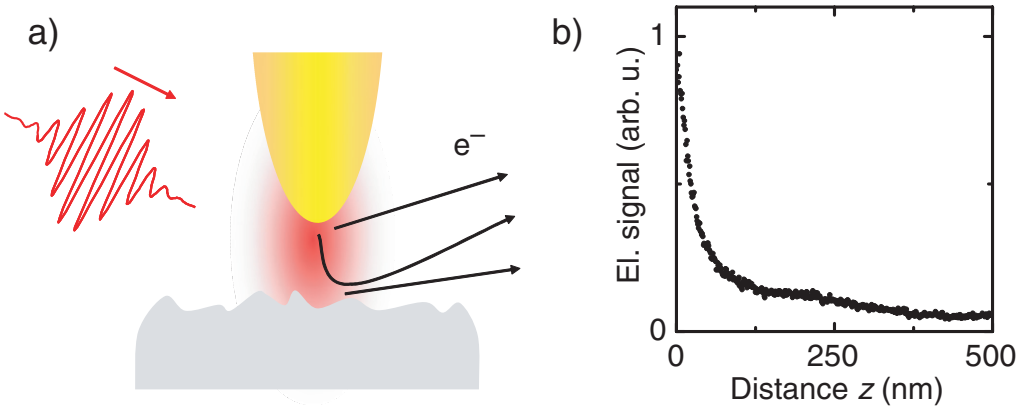

Figure 25. (a) Concept of the tip-enhanced electron emission microscope, indicating possible contrast mechanisms due to (i) a modification of the electron yield from the tip, (ii) local electron emission from the sample induced by the enhanced fields near the tip end, (iii) single or multiple scattering of electrons at the tip and/or the sample. (b) Dependence of the electron signal on the tip-to-sample distance z when approaching a gold surface.

illustrated in figure 25(a). We have recently reported the first successful implementation of such a microscope [84] and have demonstrated imaging of local electric fields in metallic nanostructures with 20 nm spatial resolution. The high spatial resolution achievable with this tip-enhanced electron emission microscope becomes apparent from the tip–sample distance dependence of the electron signal (figure 25(b)), recorded by approaching a gold surface to the illuminated metal tip. As in the unmodulated SH approach curves (figure 17(a)), one finds a gradual increase of the electron signal within the last hundreds of nanometres and then a steep increase when bringing the sample into the near-field at the tip apex. In the absence of a bias voltage, the electron signal increases by a factor of 2 within the last 20 nm. So far, we have not yet made use of the inherent temporal resolution of such a microscope. It will be interesting to explore the combined spatio-temporal resolution of this new microscope for probing the coherent ultrafast SPP dynamics in metallic nanostructures. Such studies may also allow for directly probing the time structure of the nano-sized electron pulses.

Acknowledgments

All experiments on plasmonic crystals have been performed in close collaboration with the research group of Dai-Sik Kim at Seoul National University, Korea. We wish to thank in particular D J Park, J E Kihm and K G Lee for their contributions to this work. The high quality metal nanoslit arrays studied in this work have been fabricated in the group of J Kim at Korea Research Institute of Standards and Science in Taejon, Korea. We greatly acknowledge the support of Q Han Park, Korea University, Seoul, Korea and of Roland Müller, MBI Berlin, in the theoretical analysis of plasmonic crystals. We very much thank G Steinmeyer and G Stibenz, MBI Berlin, for their advice on ultrafast lasers and pulse characterization and for their contributions to the ultrafast pulse propagation experiments. Financial support of the work in Korea by MOST and KOSEF and that at MBI in Germany by the Deutsche Forschungsgemeinschaft (SFB296) is gratefully acknowledged. We also wish to greatly thank

C-P Schulz, MBI Berlin, and D R Solli for their contributions to the electron generation experiments.

We are indebted to M Labardi, M Celebrano, D Polli and M Allegrini for the SHG experiments. G C and M Z-R acknowledge financial support from the National FIRB project 'Nanotechnologies and Nanodevices for the Information Society'.

References

[1] Raether H 1988 *Surface Plasmons on Smooth and Rough Surfaces and on Gratings* (Berlin: Springer)
[2] Konopsky V N and Alieva E V 2006 *Phys. Rev. Lett.* **97** 253904
[3] Sarid D 1981 *Phys. Rev. Lett.* **47** 1927–30
[4] Chang R K and Furtak T E (ed) 1982 *Surface Enhanced Raman Scattering* (New York: Plenum)
[5] Liebermann T and Knoll W 2000 *Colloids Surf.* A **171** 115–30
[6] Okamoto K, Niki I, Shvartser A, Narukawa Y, Mukai T and Scherer A 2004 *Nat. Mater.* **3** 601–5
[7] Köhler R, Tredicucci A, Beltram F, Beere H E, Linfield E H, Davies A G, Ritchie D A, Iotti R C and Rossi F 2002 *Nature* **417** 156–9
[8] Vaupel M, Eing A, Greulich K O, Roegener J, Schellenberg P, Striebel H M and Arlinghaus H F 2005 *Microarray Technology and Its Applications* ed D Nicolau and U Mueller (Berlin: Springer)
[9] Pokinski M and Arwin H 2004 *Thin Solid Films* **455–6** 716–21
[10] Maier S A, Kik P G, Atwater H A, Meltzer S, Harel E, Koel B E and Requicha A A G 2003 *Nat. Mater.* **2** 229–32
[11] Lezec H J, Degiron A, Devaux E, Linke R A, Martin-Moreno L, Garcia-Vidal F J and Ebbesen T W 2002 *Science* **297** 820–2
[12] Barnes W L, Dereux A and Ebbesen T W 2003 *Nature* **424** 824–30
[13] Ditlbacher H, Krenn J R, Schider G, Leitner A and Aussenegg F R 2002 *Appl. Phys. Lett.* **81** 1762–4
[14] Ebbesen T W, Lezec H J, Ghaemi H F, Thio T and Wolff P A 1998 *Nature* **391** 667–9
[15] Joannopoulos J D, Meade R D and Winn J N 1995 *Photonic Crystals* (Princeton NJ: Princeton University Press)
[16] Kim D S, Hohng S C, Malyarchuk V, Yoon Y C, Ahn Y H, Yee K J, Park J W, Kim J, Park Q H and Lienau C 2003 *Phys. Rev. Lett.* **91** 143901
[17] Dogariu A, Thio T, Wang L J, Ebbesen T W and Lezec H J 2001 *Opt. Lett.* **26** 450–2
[18] Dogariu A, Nahata A, Linke R A, Wang L J and Trebino R 2002 *Appl. Phys.* B **74** 69–73
[19] Kubo A, Onda K, Petek H, Sun Z, Jung Y S and Kim H K 2005 *Nano Lett.* **5** 1123–7
[20] Hamann H F, Gallagher A and Nesbitt D J 1998 *Appl. Phys. Lett.* **73** 1469–71
[21] Sönnichsen C, Franzl T, Wilk T, von Plessen G, Feldmann J, Wilson O and Mulvaney P 2002 *Phys. Rev. Lett.* **88** 077402
[22] Diels J-C, Van Stryland E and Benedict G 1978 *Opt. Commun.* **25** 93–5
[23] Stibenz G, Ropers C, Lienau C, Warmuth Ch, Wyatt A S, Walmsley I A and Steinmeyer G 2006 *Appl. Phys.* B **83** 511–9
[24] Walmsley I A 2004 Characterization of ultrashort optical pulses in the few-cycle-regime using spectral phase interferometry for direct electric-field reconstruction *Few-Cycle Laser Pulse Generation and Its Application* (*Topics in Applied Physics* vol 95) ed F X Kärtner (Berlin: Springer)
[25] Trebino R 2000 *Frequency-Resolved Optical Gating: The Measurement of Ultrashort Laser Pulses* (Dordrecht: Kluwer)
[26] Telle H R, Steinmeyer G, Dunlop A E, Stenger J, Sutter D H and Keller U 1999 *Appl. Phys.* B **69** 327–32
[27] Jones D J, Diddams S A, Ranka J K, Stentz A, Windeler R S, Hall J L and Cundiff S T 2000 *Science* **288** 635–9
[28] Libertun A R, Shelton R, Kapteyn H C and Murnane M M 1999 *Conf. on Lasers and Electro-Optics, OSA Technical Digest Series (Washington, DC)* paper CThR3

[29] Kowalevicz A M Jr, Zare A T, Kärtner F X, Fujimoto J G, Dewald S, Morgner U, Scheuer V and Angelow G 2003 *Opt. Lett.* **28** 1597–9
[30] Fernandez A, Fuji T, Poppe A, Fürbach A, Krausz F and Apolonski A 2004 *Opt. Lett.* **29** 1366–9
[31] Betzig E and Trautman J K 1992 *Science* **257** 189–95
[32] Karrai K and Grober R D 1995 *Appl. Phys. Lett.* **66** 1842–4
[33] Karrai K and Tiemann I 2000 *Phys. Rev.* B **62** 13174–81
[34] Giessibl F J 2003 *Rev. Mod. Phys.* **75** 949–83
[35] Reynaud F, Salin F and Barthelemy A 1989 *Opt. Lett.* **14** 275
[36] Popov E, Nevière M, Enoch S and Reinisch R 2000 *Phys. Rev.* B **62** 16100–8
[37] Martin Y C, Hamann H F and Wickramasinghe H K 2001 *J. Appl. Phys.* **89** 5774–8
[38] Cao Q and Lalanne P 2002 *Phys. Rev. Lett.* **88** 057403
[39] Lezec H and Thio T 2004 *Opt. Express* **12** 3629
[40] Lee K G and Park Q-H 2005 *Phys. Rev. Lett.* **95** 103902
[41] Genet C and Ebbesen T W 2007 *Nature* **445** 39–46
[42] Ropers C, Park D J, Stibenz G, Steinmeyer G, Kim J, Kim D S and Lienau C 2005 *Phys. Rev. Lett.* **94** 113901
[43] Hohng S C *et al* *Appl. Phys. Lett.* **81** 3239–41
[44] Ghaemi H F, Thio T, Grupp D E, Ebbesen T W and Lezec H J 1998 *Phys. Rev.* B **8** 6779–82
[45] Sarrazin M, Vigneron J P and Vigoureux J-M 2003 *Phys. Rev.* B **67** 085415
[46] Genet C, van Exter M P and Woerdman J P 2003 *Opt. Commun.* **225** 331–6
[47] Ropers C *et al* 2006 *Appl. Phys.* B **84** 183–9
[48] Ropers C 2007 *PhD Thesis* Max-Born-Institut für Nichtlineare Optik und Kurzzeitspektroskopie, Berlin
[49] Fano U 1938 *Ann. Phys.* **424** 393
[50] Fano U 1961 *Phys. Rev.* **124** 1866–78
[51] Lynch D W and Hunter W R 1998 *Handbook of Optical Constants of Solids* (New York: Academic)
[52] Johnson P B and Christy R W 1972 *Phys. Rev.* B **6** 4370–9
[53] Dicke R H 1954 *Phys. Rev.* **93** 99
[54] Lee K G *et al* 2006 *Nat. Phot.* **1** 53–6
[55] Mihalcea C, Scholz W, Werner S, Münster S, Oesterschulze E and Kassing R 1996 *Appl. Phys. Lett.* **68** 3531–3
[56] Lienau C, Richter A and Elsaesser T 1996 *Appl. Phys. Lett.* **69** 325
[57] Saiki T and Matsuda K 1999 *Appl. Phys. Lett.* **74** 2773
[58] Frey H G, Keilmann F, Kriele A and Guckenberger R 2002 *Appl. Phys. Lett.* **81** 5030
[59] Frey H G, Witt S, Felderer K and Guckenberger R 2004 *Phys. Rev. Lett.* **93** 200801
[60] Taminiau T H, Moerland R J, Segerink F B, Kuipers L and van Hulst N F 2007 *Nano Lett.* **7** 28
[61] Zenhausern F, O'Boyle M P and Wickramasinghe H K 1994 *Appl. Phys. Lett.* **65** 1623–5
[62] Hillenbrand R and Keilmann F 2000 *Phys. Rev. Lett.* **85** 3029–32
[63] Labardi M, Patanè S and Allegrini M 2000 *Appl. Phys. Lett.* **77** 621–3
[64] Hillenbrand R, Taubner T and Keilmann F 2002 *Nature* **418** 159–62
[65] Inouye Y and Kawata S 1994 *Opt. Lett.* **19** 159–61
[66] Michaelis J, Hettich C, Mlynek J and Sandoghdar V 2000 *Nature* **405** 325–8
[67] Sanchez E J, Novotny L and Xie X S 1999 *Phys. Rev. Lett.* **82** 4014–7
[68] Hartschuh A, Sanchez E J, Xie X S and Novotny L 2003 *Phys. Rev. Lett.* **90** 095503
[69] Hartschuh A, Pedrosa H N, Novotny L and Krauss T D 2003 *Science* **301** 1354–6
[70] Ropers C, Neacsu C C, Elsasser T, Albrecht M, Raschke M B and Lienau C 2007 *Nano Lett.* **7** 998
[71] Labardi M, Allegrini M, Zavelani-Rossi M, Polli D, Cerullo G, De Silvestri S and Svelto O 2004 *Opt. Lett.* **29** 62–4
[72] Zayats A V and Sandoghdar V 2000 *J. Microsc.* **202** 94–9
[73] Zayats A V, Kalbrenner T, Sandoghdar V and Mlynek J 2000 *Phys. Rev.* B **61** 4545–8

[74] Bouhelier A, Beversluis M, Hartschuh A and Novotny L 2003 *Phys. Rev. Lett.* **90** 013903
[75] Neacsu C C, Reider G A and Raschke M B 2005 *Phys. Rev.* B **71** 201402
[76] Kawata Y, Xu C and Denk W 1999 *J. Appl. Phys.* **85** 1294–301
[77] Beversluis M R, Bouhelier A and Novotny L 2003 *Phys. Rev.* B **68** 115433
[78] Fischer U Ch and Zingsheim H P 1981 *J. Vac. Sci. Technol.* B **19** 881–5
[79] Bechtel J H, Lee Smith W and Bloembergen N 1977 *Phys. Rev.* B **15** 4557–63
[80] Yen R, Liu J and Bloembergen N 1980 *Opt. Commun.* **35** 277–82
[81] Keldysh L V 1965 *Sov. Phys—JETP* **20** 1307
[82] Corkum P B, Burnett N H and Brunel F 1989 *Phys. Rev. Lett.* **62** 1259–62
[83] Hommelhoff P, Sortais Y, Talesh A A and Kasevich M A 2006 *Phys. Rev. Lett.* **96** 077401
[84] Ropers C, Solli D R, Schulz C P, Lienau C and Elsaesser T 2007 *Phys. Rev. Lett.* **98** 043907
[85] Ihee H, Lobastov V A, Gomez U M, Goodson B M, Srinivasan R, Ruan C-Y and Zewail A H 2001 *Science* **291** 458–62
[86] Siwick B J, Dwyer J R, Jordan R E and Dwayne Miller R J 2003 *Science* **302** 1382–5
[87] Ruan C-Y, Murooka Y, Raman R K and Murdick R A 2007 *Nano Lett.* **7** 1290–6
[88] Lobastov V A, Srinivasan R and Zewail A H 2005 *Proc. Natl. Acad. Sci. USA* **102** 7069–73
[89] King W E, Campbell G H, Frank A, Reed B, Schmerge J F, Siwick B J, Stuart B C and Weber P M 2005 *J. Appl. Phys.* **97** 111101
[90] Fowler R H and Nordheim L W 1928 *Proc. R. Soc. Lond.* A **119** 173
[91] Gasiorowicz S 2003 *Quantum Physics* 3rd edn (New York: Wiley)
[92] Burgess R E, Kroemer H and Houston J M 1953 *Phys. Rev.* **90** 515
[93] Spindt C A, Brodie I, Humphrey L and Westerberg E R 1976 *J. Appl. Phys.* **47** 5248–63
[94] Berdinsky A S, Shaporin A V, Yoo J-B, Park J-H, Alegaonkar P S, Han J-H and Son G-H 2006 *Appl. Phys.* A **38** 377
[95] Petek H and Ogawa S 1997 *Prog. Surf. Sci.* **56** 239–310
[96] Aeschlimann M, Bauer M and Pawlik S 1996 *Chem. Phys.* **205** 127–41
[97] Quinn J J 1962 *Phys. Rev.* **126** 1453–7
[98] Hommelhoff P, Kealhofer C and Kasevich M A 2006 *Phys. Rev. Lett.* **97** 247402
[99] Anisimov A I, Benderskii V A and Farkas G 1977 *Sov. Phys—Usp.* **20** 467
[100] Pomraenke R, Ropers C, Renard J, Lienau C, Lüer L, Polli D and Cerullo G 2007 *Nano Lett.* **7** 998–1002
[101] Ruan C Y, Vigliotti F, Lobastov V A, Chen S and Zewail A H 2004 *Proc. Natl Acad. Sci. USA* **101** 1123–8